10
Simple Fluids in Nanochannels

With the growing interest in the development of faster, smaller, and more efficient biochemical analysis devices, nanofluidic systems and hybrid micro/nano fluidic systems have attracted considerable attention in recent years. In nanoscale systems, the surface-to-volume ratio is very high, and the critical dimension can be comparable to the size of the fluid molecules. The influence of the surface and the finite-size effect of the various molecules on fluid transport needs to be understood in detail, while such effects may be largely neglected for liquid flows in macroscopic channels. In this chapter, we discuss the analysis of simple fluids such as Lennard–Jones liquids in confined nanochannels. A key difference between the simulation of the fluidic transport in confined nanochannels, where the critical channel dimension can be a few molecular diameters, and at macroscopic scales is that the well-established continuum theories based on Navier–Stokes equations may not be valid in confined nanochannels. Therefore, atomistic scale simulations, in which the fluid atoms are modeled explicitly or semiexplicitly and the motion of the fluid atoms is calculated directly, shed fundamental insights on fluid transport. The most popular technique for atomistic simulation of liquid transport is molecular dynamics (MD), which is discussed in detail in Chapter 16. After presenting some details on the atomistic simulation of simple fluids, we discuss density profiles, diffusion transport, and validity of the Navier–Stokes equations for simple fluids in confined nanochannels. In the last section we discuss in detail the slip condition at solid–liquid interfaces and present experimental and computational results as well as conceptual models of slip. We also revisit the lubrication problem, first discussed in Chapter 7, and we present the Reynolds–Vinogradova

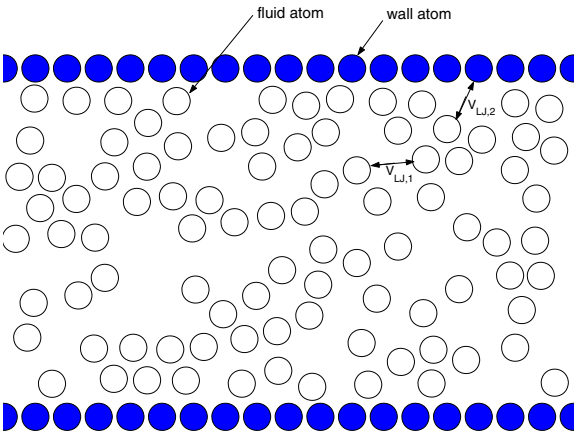

FIGURE 10.1. A sketch of a nanochannel filled with a simple fluid. The filled circles denote the channel wall atoms, and the open circles denote the fluid atoms. The fluid atoms interact with each other by a Lennard–Jones potential $V_{LJ,1}$, and the fluid atoms interact with the wall atoms by a Lennard–Jones potential $V_{LJ,2}$.

theory for hydrophobic surfaces.

10.1 Atomistic Simulation of Simple Fluids

Atomistic simulation of nanofluids has gained considerable attention over the last two decades. Much of the existing literature has been devoted to understanding "simple fluids" in nanochanels. Though there is no consensus on the precise definition of a simple fluid in the literature, in most cases, it is simply taken as a collection of atoms that interact via the Lennard–Jones potential and the dynamics of which follow the classical mechanics described by Newton's law. In practice, some noble gases (e.g., argon) can be modeled fairly accurately as a simple fluid. Figure 10.1 shows a schematic of a nanochannel filled with a simple fluid.

The investigation of simple fluids, in contrast to the study of complex fluids such as water (discussed in Chapter 11) or electrolytes (discussed in Chapter 12), has many advantages. First, the computational cost of atomistic simulation involving simple fluids is much lower compared to that of complex fluids, since it is much cheaper to evaluate the Lennard–Jones potential describing simple fluids compared to the evaluation of the electrostatic interactions that are required in the study of most complex fluids. Second, despite its simplicity, the investigation of simple fluids can provide deep insight into the physics of fluid transport in nanochannels, and such insight can guide the study of more complex fluids. For example, the

study of simple fluids indicated that the classical Navier–Stokes equations breakdown in a channel as narrow as 4 fluid atomic diameters (Travis et al., 1997), and later, a similar finding was reported for electroosmotic transport in a silicon nanochannel that is also about 4 water diameters wide (Qiao and Aluru, 2003b). Third, the investigation of simple fluid transport provides data for the validation of theories describing fluid transport in nanochannels. Due to the complicated interactions involved in complex fluids, most of the nanofluid transport theories that have been developed so far are limited to simple fluids.

As mentioned above, simple fluids can be described using a Lennard–Jones (LJ) potential (LJ and other potentials are discussed in detail in Section 16.1; here we quickly recap the salient features of the LJ potential and introduce the reduced units that are used in this chapter) of the form

$$V_{LJ} = 4\epsilon \left[\left(\frac{\sigma}{r} \right)^{12} - \left(\frac{\sigma}{r} \right)^{6} \right], \tag{10.1}$$

where ϵ, σ are the Lennard–Jones parameters that depend on the atoms involved in the interaction. Note that:

1. ϵ is related to the interaction strength, and a higher ϵ corresponds to a higher interaction energy between the atoms.

2. σ corresponds to the distance at which the potential between the two atoms goes to zero, which can be approximately taken as the diameter of a fluid atom.

Since the Lennard–Jones potential describes the interactions between non polar molecules quite well (Talanquer, 1997) and the force corresponding to the Lennard–Jones potential can be evaluated efficiently numerically, it is the most popular interaction potential used in MD simulations. In the MD simulation of Lennard–Jones fluids, the physical quantities are typically computed using reduced units. Table 10.1 summarizes the units for various quantities, e.g., length, temperature, and density. In the table, ϵ and σ are as defined in equation (10.1), k_{B} is the Boltzmann constant, and m is the mass of a Lennard–Jones atom. Unless otherwise mentioned, all the quantities are measured in reduced units in the next two sections.

The studies on Lennard–Jones fluids have indicated that depending on the critical length scale of the channel (typically the channel width/height or the diameter), the fluidic transport behavior (e.g., convection and diffusion phenomena) can either deviate significantly from the classical continuum theory prediction or be very similar to the transport of a bulk fluid described by the classical theory. These observations follow from the fact that when the fluid atoms are confined to molecular channels, the fluid can no longer be taken to be homogeneous, and strong oscillations in fluid density occur near the solid–fluid interface. Therefore, the dynamic behavior of the fluid becomes significantly different from that of the bulk. Some

TABLE 10.1. Units for various quantities in Lennard–Jones fluids.

Length	σ	Velocity	$(\epsilon/m)^{1/2}$
Mass	m	Shear rate	$(\epsilon/m\sigma^2)^{1/2}$
Energy	ϵ	Stress	ϵ/σ^3
Time	$(m\sigma^2/\epsilon)^{1/2}$	Viscosity	$(m\epsilon)^{1/2}/\sigma^2$
Number density	σ^{-3}	Diffusivity	$\sigma(\epsilon/m)^{1/2}$
Temperature	ϵ/k_B		

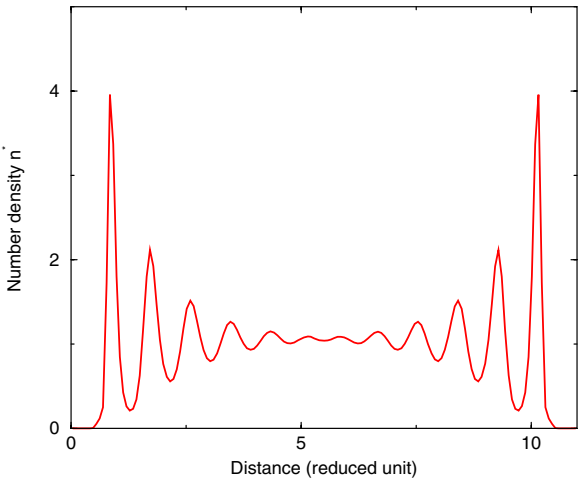

FIGURE 10.2. Density profile of a Lennard–Jones fluid. Simulations are performed in an 11-fluid-atomic-diameter channel.

significant results that have been observed when LJ liquids are confined in nanochannels are summarized below.

10.2 Density Distribution

The strong density oscillations of fluid atoms near the fluid/solid interface is a universal phenomenon, and it has been observed in almost all MD simulations of nanofluidic flows and been verified experimentally (Chan and Horn, 1985; Zhu and Granick, 2002; Zhu and Granick, 2001). Figure 10.2 shows the density profile of Lennard–Jones fluid atoms in a 11-fluid-diameter-wide channel (see also Figure 1.7, which shows density fluctuations of an LJ liquid in a larger channel). Density fluctuations near a channel wall can be explained using the concept of a radial distribution function (RDF). A radial distribution function (or the pair correlation function), typically denoted

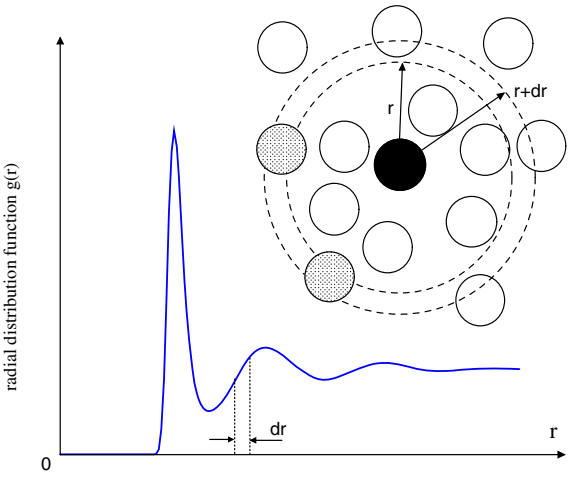

FIGURE 10.3. Sketch of a typical radial distribution function (RDF) $g(r)$. RDF measures the probability density of finding a particle at a distance r from a given particle ($r = 0$ corresponds to the position of the given particle).

by $g(r)$, is a basic measure of the structure of a liquid. RDF measures the probability density of finding a particle at a distance r from a given particle position. Figure 10.3 is a sketch of a typical radial distribution function. At a short distance from the given particle position, $g(r)$ is essentially zero because of the strong repulsion between the particles; i.e., particles cannot get too close to each other. As r increases, $g(r)$ shows a first peak, which is mainly caused by the attractive interactions between the particles. At a short distance from the first peak, a depletion of the particles is observed because of repulsive forces, and this gives rise to a minimum in $g(r)$. The combination of the attractive and the repulsive forces between the particles leads to the various peaks and valleys observed in the radial distribution function shown in Figure 10.3. At a distance farther away from the given particle position, the distribution of particles is no longer influenced by the given particle, and $g(r)$ approaches a constant. The fluid layering near the channel wall is mainly induced by the structure of the fluid radial distribution function and the structure of the solid wall. Here the position of the solid wall is similar to the position of the given particle in the radial distribution function, and the fluid density oscillations are similar to the oscillations in the radial distribution function.

Simple fluids in nanochannels are inhomogeneous because of the strong layering of fluid atoms near the channel wall. Classical fluid transport theories do not account for the inhomogeneity of the fluid, and transport parameters such as diffusivity and viscosity are strongly influenced by the fluid layering in nanochannels (Thompson and Troian, 1997). Fluid lay-

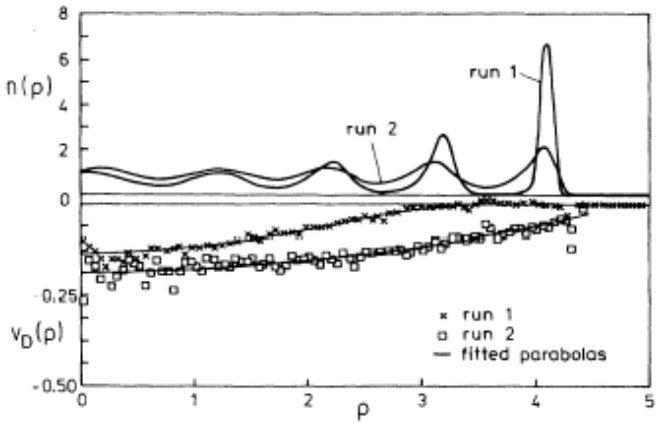

FIGURE 10.4. Density (upper panel) and velocity (lower panel) profiles in a 5.0σ-radius cylindrical pore for two separate runs with different wall–fluid interactions. In the first run, ϵ_{wf} is 3.5 times larger than ϵ, and in the second run, ϵ_{wf} is equal to ϵ. (Courtesy of J. Fischer.)

ering can be influenced by various parameters such as the wall structure, fluid–wall interactions, and channel width, and these issues are discussed below.

Effect of Fluid–Wall Interactions

The interaction between a fluid atom and a wall atom is usually modeled by the Lennard–Jones potential. The Lennard–Jones parameters for fluid–fluid and fluid–wall interactions are denoted by (ϵ, σ) and $(\epsilon_{\mathrm{wf}}, \sigma_{\mathrm{wf}})$, respectively. A higher ϵ_{wf} corresponds to a stronger interaction between the fluid and the wall atoms. (Heinbuch and Fischer, 1989) found that the fluid layering becomes stronger when ϵ_{wf} increases. Figure 10.4 shows the number density and velocity profiles for two separate runs with different fluid–wall interaction parameters in a 5.0-σ radius cylindrical pore. In the first run, ϵ_{wf} is 3.5 times larger than ϵ, and in the second run, ϵ_{wf} is equal to ϵ. In both runs, the average number density of the fluid in the pore is 0.8 and the temperature of the fluid is 0.835. Clearly, the layering effect is much more distinct in the first run compared to the second run. This can be explained by the fact that as ϵ_{wf} increases, the attractive force exerted by the wall atoms on the fluid atoms increases, and the tendency of a fluid atom to stay near the wall increases. A similar observation has been made by (Thompson and Robbins, 1990) in their study of Couette flow in a slit channel of width 12.8σ.

(Travis and Gubbins, 2000) further investigated the variation of the density profile in a nanochannel when the attractive part of the Lennard–Jones

interaction is turned *on* and *off* by shifting the Lennard–Jones potential. Specifically, the Poiseuille flow in a 4.0σ-wide slit channel was investigated for three different systems, A, B, and C. In system A, fluid–fluid and fluid–wall interactions are described by the purely repulsive part of the Lennard–Jones, or Weeks–Chandler–Andersen (WCA) potential (see Section 16.1 for details on WCA potential). In system B, the fluid–fluid and fluid–wall interactions are described by the full 12-6 Lennard–Jones (including both the attractive and the repulsive interactions) potential. In system C, the fluid–fluid interactions are described by the WCA potential, and the interactions between the fluid and the wall are described by the full 12-6 Lennard–Jones potential. Figure 10.5 (a) shows a comparison of the density profiles for the three different systems. It is observed that the presence of attractive fluid–wall forces (system B and C) leads to the formation of boundary liquid layers of higher density than in the case of repulsive wall–fluid interactions (system A). It is also observed that the density of the layers is higher in system C compared to that of system B. This can be explained by the fact that compared to system B, the fluid atoms in system C have a greater affinity for the wall atoms and less affinity for other fluid atoms. In addition, the number of density peaks (i.e., the number of fluid layers in the channel) is also different for the three systems. These results indicate that the density distribution of fluid atoms in the channel is sensitive to both the fluid–wall and fluid–fluid interactions, and care should be taken in choosing the best potential to depict a particular fluidic system. Figure 10.5 (b) shows the average number density of fluid atoms along the channel length direction. We see that the fluids are highly structured in all three systems. The density oscillates with a wavelength of order σ. Clearly, the wall structure has been imposed upon the fluid. Similar behavior has also been observed by (Zhang et al., 2001) in the simulation of n-decane confined between two Au(111) surfaces.

Effect of Structure and Thermal Motion of the Wall Atoms

Smooth walls (Toxvaerd, 1981; Somers and Davis, 1992) as well as walls with atomistic structure (Travis and Gubbins, 2000; Sokhan et al., 2001; Somers and Davis, 1992) have been widely used in the MD simulation of fluids confined in nanoscale channels. For a smooth wall, the wall–fluid potential depends only on the normal distance between the fluid atom and the channel wall, while for a wall with atomistic structure, the wall–fluid potential depends on the relative distance between the fluid atom and each atom in the wall. Typically, only the first fluid layer is significantly influenced by the wall structure, and the rest of the fluid layers are not significantly affected by the structure of the wall. In many simulations, the wall atoms are either frozen to their lattice sites (Heinbuch and Fischer, 1989; Zhang et al., 2001) or constrained to their lattice sites by a spring (Thompson and Robbins, 1990; Travis and Gubbins, 2000; Sokhan et al., 2001). The former

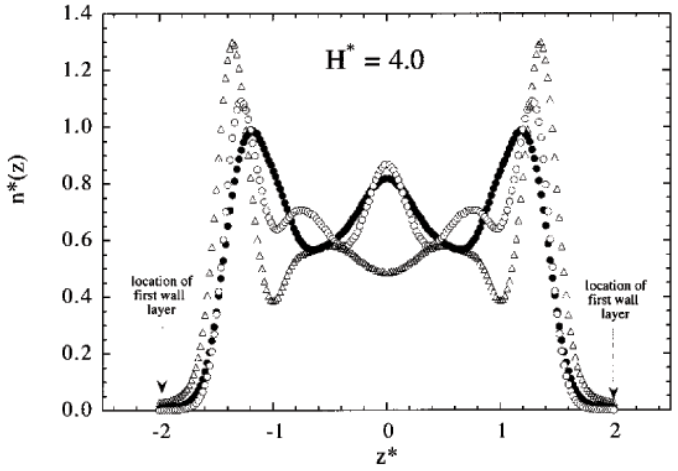

(a)

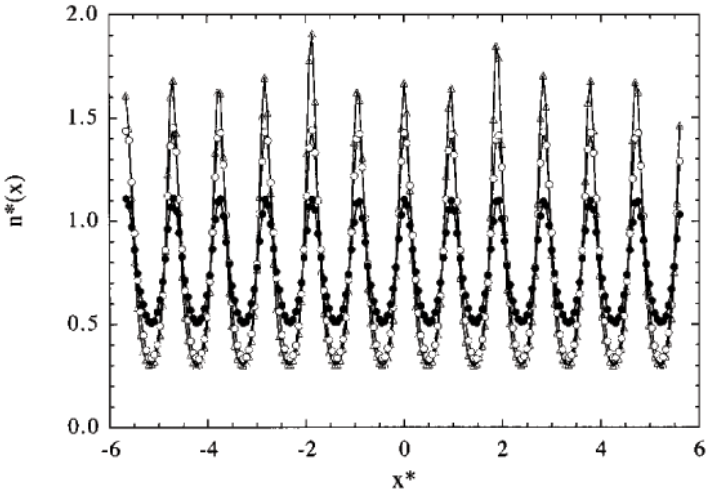

(b)

FIGURE 10.5. Number density profiles across (a) and along (b) a 4.0σ-wide slit channel for three different cases where the fluid–fluid and fluid–wall interactions are modeled differently (System A: WCA system, filled circles, system B: LJ system, open circles, and system C: WCA-LJ system, open triangles). (Courtesy of K. P. Travis.)

enables the use of a larger time step in MD, since the thermal vibration of the solid atoms is not resolved, while the latter seems to be more realistic. The thermal oscillation of wall atoms introduces further corrugations into the potential felt by the fluid atoms near the wall, and therefore leads to a reduced density oscillation near the channel wall (Thompson and Robbins, 1990; Sokhan et al., 2001).

Effect of Channel Width

The density oscillations in the channel also depend on the channel width. Somers and Davis investigated the variation of density profiles in slit channels of different widths ranging from 2.0σ to 8.0σ (Somers and Davis, 1992). Figure 10.6 shows the density profiles obtained with various channel widths. The results indicate that for channel widths that can accommodate integral fluid layers, e.g., 2σ, 2.75σ, and 4σ, distinct peaks in the density profile are observed. For channel widths, such as 2.25σ and 3.25σ, the channel is wide enough to accommodate distinct fluid layers: hence additional layers begin to develop, and the new layers appear at channel widths of 2.5σ and 3.5σ. When the channel width is 8σ, seven distinct peaks are observed, and as the channel width increases further, more peaks are observed, but these additional peaks are much weaker compared to the peaks very close to the channel wall. For channels wider than 10σ, the fluid layers near the wall are independent of the channel width, and the fluid in the central portion of the channel behaves more like a bulk fluid.

Effect of Fluid Flow

The fluid flow is found to have negligible effect on the density distribution. (Bitsanis et al., 1987) conducted simulations on Couette flow in a nanometer-slit pore using shear rates of 10^{10} to 10^{11} s^{-1} and found that the density distribution is not significantly influenced by the flow; i.e., the density profile in the channel in the presence of bulk transport of fluid is the same as that obtained from an equilibrium MD simulation. This result was also verified by other reported MD simulations. Since experimental techniques or real processes that deal with fluid flow in nanopores are likely to employ smaller shear rates than those that were employed in MD, we can conclude that in simple fluids the density profile will be the equilibrium density profile.

While all the results presented above on the calculation of density profiles in nanochannels were based on MD simulations, the density profiles can also be calculated using analytical methods. (Fischer and Methfessel, 1980) as well as (Bitsanis et al., 1988) have used the Yvon–Born–Green (YBG) theory (McQuarrie, 1973) of inhomogeneous fluids with the Fischer–Methfessel approximation for the fluid pair-correlation functions (Fischer and Methfessel, 1980) to calculate the density distribution of Lennard–Jones atoms confined in a nanoscale channel. In order to obtain an equation for number

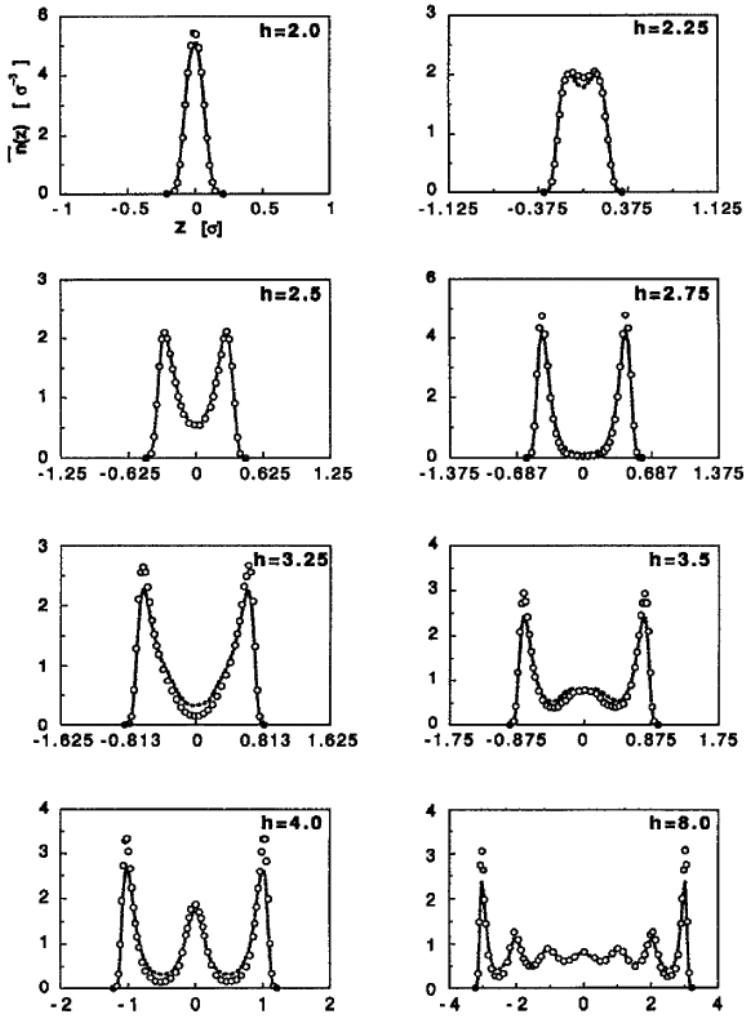

FIGURE 10.6. Fluid density distribution in smooth-slit channels of different widths. The results with reservoir are shown as a line, and the results with no reservoir are shown as circles. A reservoir is introduced to simulate the Couette flow. (Courtesy of H. T. Davis.)

density one has to approximate the pair correlation function, which is the Fischer–Methfessel approximation. This is the only approximation needed, and in this respect the YBG theory is superior to the free-energy theories. The YBG theory has been shown to predict the fluid densities near smooth

walls with good accuracy.

10.3 Diffusion Transport

Diffusion transport is typically important in most nanofluidic systems. This can be understood by calculating the Peclet number, $P_e = UL/D$, which measures the ratio of the bulk transport (convection) to the diffusion transport. In most nanofluidic systems, the characteristic length L ranges from a nanometer to a micrometer, and the bulk velocity ranges from a micrometer per second to a millimeter per second. For a fluid with a diffusivity of $D = 1.0 \times 10^{-9}$ m/s^2, the Peclet number ranges from 10^{-6} to 1, indicating that diffusion either dominates the transport or is as important as the bulk transport.

The diffusion coefficient must be generalized in order to describe transport in confined nanochannels. For *homogeneous* and *equilibrium* systems, the diffusion coefficient can be calculated using either the Green–Kubo equation

$$D = \frac{1}{3} \int_0^\infty \langle \boldsymbol{v}(0) \cdot \boldsymbol{v}(t) \rangle \, dt, \tag{10.2}$$

where $\boldsymbol{v}$ is the atom velocity and $\langle\rangle$ denotes the ensemble average, or by the Einstein equation

$$D = \frac{1}{6} \lim_{t \to \infty} \frac{\langle [\boldsymbol{r}(t_0 + t) - \boldsymbol{r}(t_0)]^2 \rangle}{t}, \tag{10.3}$$

where $\boldsymbol{r}$ is the atom position. The Green–Kubo expression given in equation (10.2) is strictly valid only for homogeneous and equilibrium systems. However, it is generally accepted that, at least for the calculation of the average diffusivity in nanochannels, the Green–Kubo expression given in equation (10.2) or the Einstein relationship given in equation (10.3) is adequate. For example, Bitsanis and coworkers (Bitsanis et al., 1987) computed pore-averaged diffusitives and found that the diffusivities under flow and the equilibrium diffusivity agree within the limits of statistical uncertainty. Moreover, the diffusivities calculated from the Green–Kubo formula and the Einstein relationship agree quite well. It is important to note that in the calculation of the diffusivities under flow, the drift contribution to either equation (10.2) or equation (10.3) has to be excluded. In summary, both the Green–Kubo formula and the Einstein relationship are widely used in the calculation of diffusivity of fluids in nanochannels.

The diffusion of fluids confined in nanoscale channels has been studied extensively in slit and cylindrical pores. In a slit pore, diffusion is different in the direction parallel (the x- and y-directions) and normal (z-direction) to the pore wall, especially for narrow pores. This is because, unlike the

diffusion parallel to the pore wall, the diffusion in the direction normal to the pore wall is inherently transient; i.e., in the long time limit, the diffusivity in the direction normal to the pore wall is zero due to the geometrical limit. To circumvent this problem, the diffusion in the z-direction is usually characterized by a mean-square displacement $\Delta z^2(t)$ that can be calculated for a short time. In this section, we will discuss the results for diffusion parallel to the pore wall (characterized by $D_{\parallel}$ or D_x and D_y) and the diffusion normal to the pore wall (characterized by $\Delta z^2(t)$) separately.

(Magda et al., 1985) studied diffusion in slit pores with smooth pore walls using equilibrium MD simulations. Figure 10.7 shows the variation of the pore-averaged diffusivity parallel to the pore ($D_{\parallel}$) with the pore width. The plot indicates that:

1. Even for the smallest pore width ($h = 2$), where the fluids are highly confined, the fluid atoms maintain considerable mobility.

2. When the channel width is small ($h < 4$), the average $D_{\parallel}$ in the pore fluctuates with the channel width, and when the channel width increases beyond $h = 5$, the average $D_{\parallel}$ increases smoothly toward the asymptotic bulk value.

3. For a channel width of $h = 11.57$, the average $D_{\parallel}$ is almost the same as the bulk diffusivity.

The second observation can be attributed to the average density variation with the change in channel width. As shown in Figure 10.7, when the channel width is small ($h < 4$), the average density fluctuates with the channel width, and when the channel width increases beyond $h = 5$, the average density decreases smoothly toward the asymptotic bulk value. The dependence of the diffusivity on density in the pore region is much weaker compared to the quadratic dependence observed in the bulk (Levesque and Verlet, 1970). This means that the variation of diffusivity with density follows a quadratic dependence as the pore width increases and the properties of the confined fluid approach that of the bulk. However, when the pore width is low (lower than 6σ), then the layering effect dominates and affects the variation of diffusivity. This leads to a weaker dependence of diffusivity on density for narrow pores. A possible explanation for this is the structured, almost solid-like form of the density profile in narrow pores.

To investigate the effect of the local fluid density on the diffusivity parallel to the pore ($D_{\parallel}$), the pore ($h = 11.57$) has been divided into five slices parallel to the solid–liquid interface, and the diffusivity $D_{\parallel}$ is calculated inside each slice. Figure 10.8 shows the density profile and the diffusivity in each slice. Clearly, even though there is a significant variation in the fluid density, the diffusivity in each slice is within the statistical error of those of the others. To understand this result in more detail, an empirical theory, *local average density method* (LADM), has been developed to describe the transport coefficient (e.g., diffusivity) of a fluid confined in a nanochannel

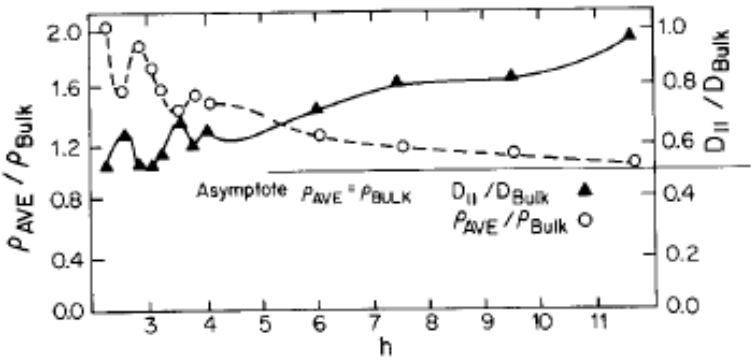

FIGURE 10.7. Correlation of the pore-averaged diffusivity parallel to the wall ($D_{\parallel}$) with the average fluid density. Here h is the pore width (reduced unit); $\rho_{\text{ave}}/\rho_{\text{bulk}}$ is the average density of the occupied pore volume divided by the density of the bulk liquid. (Courtesy of H.T. Davis.)

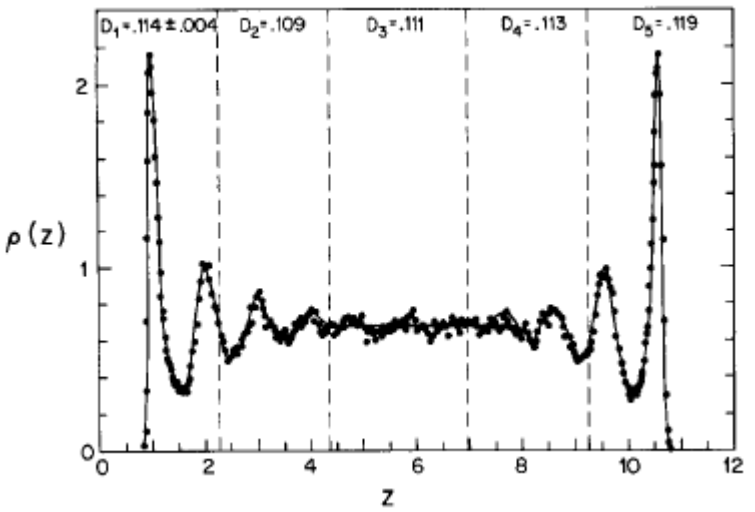

FIGURE 10.8. Diffusivity as a function of the distance from the pore walls. Here D_i is the diffusion coefficient parallel to the pore walls averaged over the ith slice parallel to the interface. The pore width is 11.57σ. (Courtesy of H.T. Davis.)

(Bitsanis et al., 1988). In the LADM theory, the diffusivity of the fluid at a position $\boldsymbol{r}$ depends on the *local average* density $\overline{\rho}(\boldsymbol{r})$ of the fluid instead of the *local* density $\rho(\boldsymbol{r})$. The local average density at $\boldsymbol{r}$ is defined as the average density inside a sphere with its center at $\mathbf{r}$ and with diameter equal

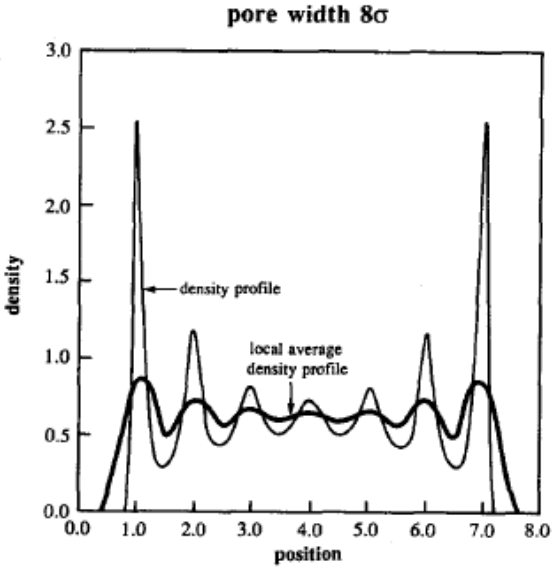

FIGURE 10.9. Density and local average density profiles in an 8σ-wide slit pore. (Courtesy of H.T. Davis.)

to the diameter of the fluid molecules σ, i.e.,

$$\overline{\rho}(\boldsymbol{r}) = \frac{1}{\pi\sigma^3/6} \int_{s<\sigma/2} \rho(\boldsymbol{r}+\boldsymbol{s})\, d^3s.$$

Figure 10.9 shows the local average density distribution in an 8.0σ channel (Bitsanis et al., 1988). Clearly, even though the oscillations in the local fluid density are significant, the local average density shows very little oscillation. This explains the small diffusivity variation in the pore (see Figure 10.8) even though there is a significant variation in the local fluid density. From the above discussion, we can conclude that in confined nanopores the parallel diffusivity at a given position is determined primarily by the average density in the pore and not by the local density.

To investigate the effect of the wall structure on the diffusivity parallel to the pore wall, (Somers and Davis, 1992) performed diffusivity calculations by considering structured and smooth walls. Figures 10.10 (a) and (b) show the variation of the diffusivity $D_{\|}$ with the pore width for the structured and smooth walls, respectively. The results for the smooth-pore wall (panel (b)) agree qualitatively with those reported in (Magda et al., 1985), and the results for the structured wall show some interesting differences from the results for the smooth wall; i.e., as the pore width increases, the diffusivity in the structured pore approaches the bulk value more slowly compared to

the smooth wall. This can be explained by the added fluid ordering in the structured pore. Figure 10.10 also shows the variation of the diffusivity with bulk transport of the fluid. For both the smooth and structured pore walls, the presence of Couette flow does not change the diffusivity noticeably for a shear rate less than $0.20\sqrt{\epsilon/m\sigma^2}$, but the diffusivity increases considerably for shear rates higher than $0.20\sqrt{\epsilon/m\sigma^2}$. It is likely that shear thinning may be responsible for the observed increase in the diffusivity. Similar results have also been observed by (Bitsanis et al., 1987). In addition, the inset in Figure 10.10 (a) shows that the wall registry (characterized by the wall registry index α) also affects the diffusivity significantly in narrow pores. This is likely to be caused by the changed fluid structure when the wall structure is varied. The wall registry is a measure of the variation in surface roughness of the wall (Somers and Davis, 1992). When the axial coordinate of the surface atoms on both the walls (i.e., the upper wall and the lower wall of the slit) are the same, then the wall registry index α is 0. However, when the upper wall atoms and the lower wall atoms are seperated by a certain distance, then the wall registry index is nonzero.

As mentioned above, the diffusivity normal to the channel wall cannot be defined using equation (10.2) or (10.3). However, it is possible to characterize the diffusion process normal to the channel wall by a mean-square displacement $\Delta z^2(t)$ that can be calculated for a short time. Figure 10.11 shows the comparison of the mean-square displacement in the direction normal (z-direction) and parallel to the channel wall (x- and y-directions) for channel widths of 3.0σ and 4.0σ. Figure 10.11 indicates that:

1. After 2.0 ps, the diffusion process in the z-direction can be characterized by a mean-square displacement.

2. The diffusion process in the z-direction is faster in the larger channel ($h = 4\sigma$) compared to the smaller channel ($h = 3\sigma$).

3. For $h = 4\sigma$, the diffusion in the x- and y-directions is much faster compared to the diffusion in the z-direction.

These results are not surprising, since the movement of the fluid atoms is more confined in the direction normal to the channel wall compared to the movement of the fluid in the direction parallel to the channel wall.

In the discussion so far, we have assumed that the fluid molecule size is smaller than half of the slit pore width and that the diffusion is characterized by the normal-mode diffusion; i.e., the mean-square displacement of the fluid molecules obeys the Einstein relationship. In the normal-mode diffusion, one molecule can pass another molecule within the channel. However, if the pore width decreases further and the pore is cylindrical, a molecule cannot pass another molecule because of its large size relative to the pore size, and the diffusion process is then characterized by a single-file diffusion. The mean-square displacement of a fluid molecule due to single-file

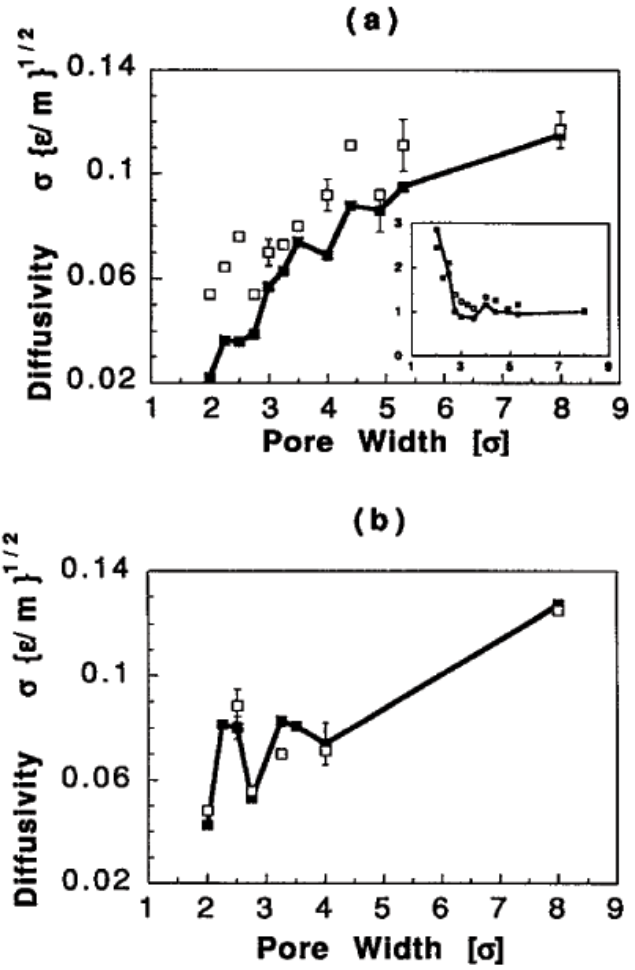

FIGURE 10.10. Diffusivity parallel to pore walls versus pore width (■ - equilibrium ($\alpha = 0$), □ - Couette flow). (a) Structured pores (inset: □ - ratio of the diffusivity in Couette flow and in equilibrium simulation ($\alpha = 0$), ■ - ratio of diffusivity in equilibrium for $\alpha = 0.71$ and $\alpha = 0$. See (Somers and Davis, 1992), for the definition of the wall registry index α). (b) Smooth pores. (Courtesy of H.T. Davis.)

diffusion can be expressed as

$$s^2 = 2Bt^{0.5},$$

where B is the diffusion mobility. For the diffusion of methane, ethane,

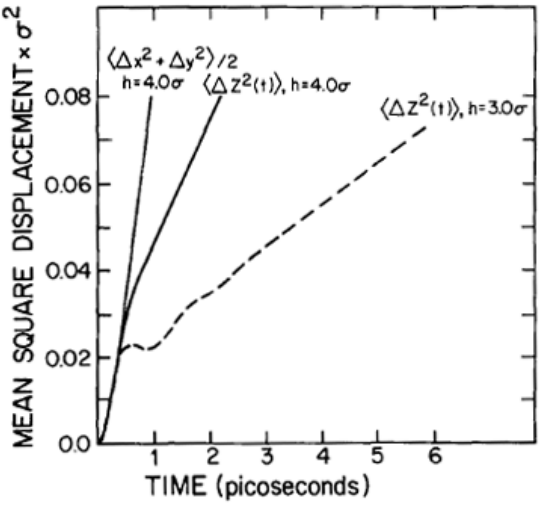

FIGURE 10.11. Comparison of the mean-square displacement parallel and normal to the channel walls. (Courtesy of H.T. Davis.)

and ethylene through carbon nanotubes (see Section 13.2 for a discussion on carbon nanotubes), (Mao and Sinnott, 2000) showed that there exists a transition-mode diffusion for which the mean-square displacement of a fluid molecule due to a single-file diffusion can be expressed as

$$s^2 = 2Ct^n.$$

Figure 10.12 shows the log-log plots of the mean-square displacement for methane, ethane, and ethylene in a $(10, 0)$ carbon nanotube (diameter: 0.8 nm). Clearly, the diffusion of methane is a normal-mode diffusion and the diffusions of ethane and ethylene are transition-mode diffusions. Mao and Sinnott further showed that the diffusion of ethane and ethylene in a $(9, 0)$ carbon nanotube (diameter: 0.72 nm) follows the single-file mode, while the diffusion of methane is still in the normal mode. Such differences are caused by the fact that the size of ethane and ethylene are larger compared to methane; therefore, the methane molecules can pass one another in a 0.72-nm diameter, while ethane and ethylene molecules cannot pass each other in such small-diameter tubes.

10.4 Validity of the Navier–Stokes Equations

In the continuum fluid transport theory governed by the Navier–Stokes equations, it is assumed that the state variables (e.g., density and tempera-

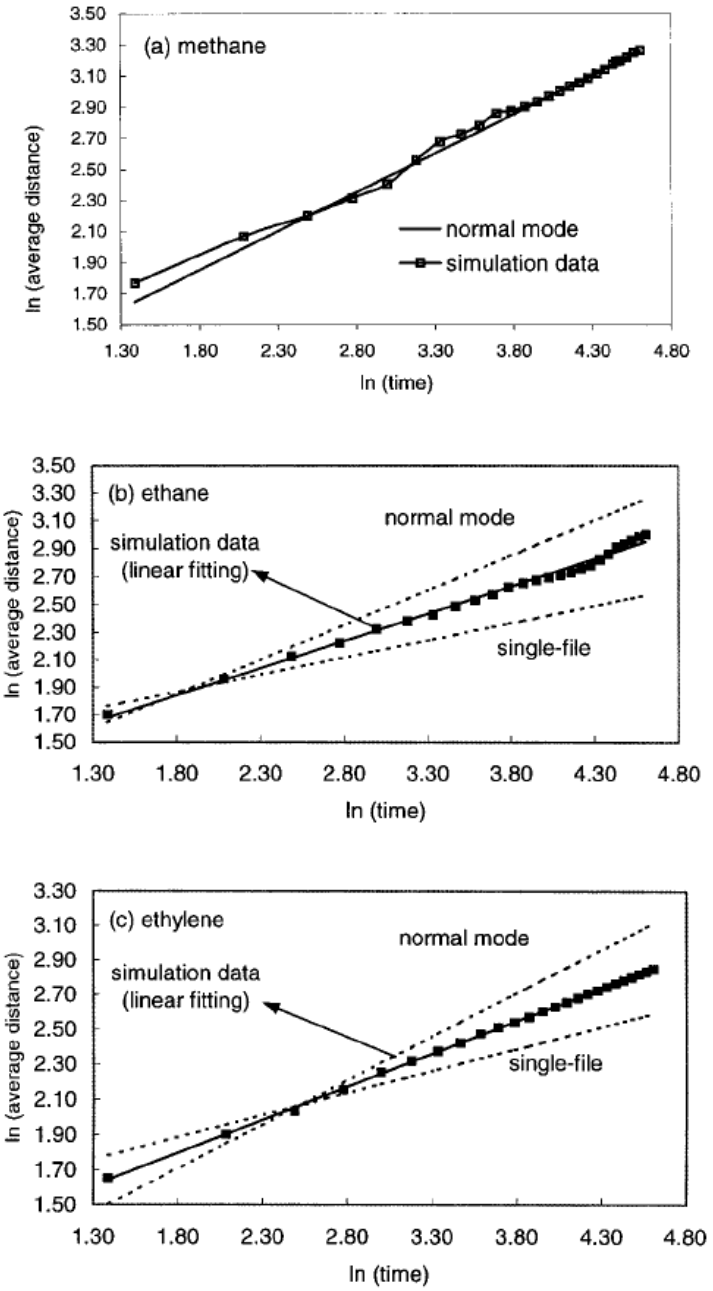

FIGURE 10.12. Log-log plot of the mean-square displacement for methane (a), ethane (b), and ethylene (c) in a $(10, 0)$ carbon nanotube (diameter: 0.8 nm). (Courtesy of S. Sinnott.)

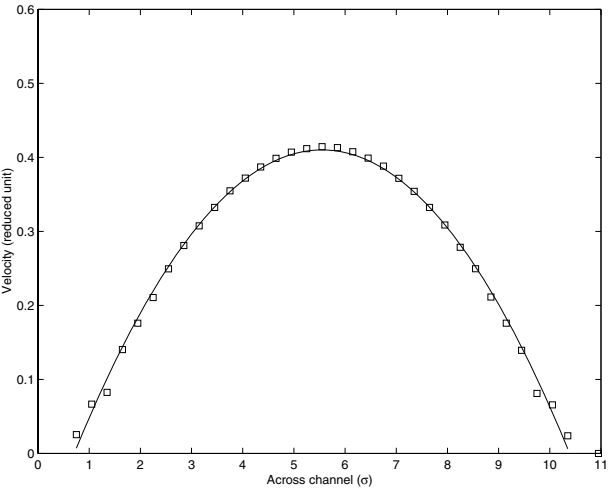

FIGURE 10.13. Velocity profile obtained from MD simulation of Poiseuille flow in an 11-fluid-diameter channel. The solid line is a quadratic fit to the velocity profile. The temperature of the fluid is set to 2.5, the average fluid density is 0.8, and a constant force of 0.1 is applied on each fluid molecule to generate the flow. All the variables are measured in reduced units.

ture) do not vary appreciably over the length and time scales comparable to the molecular free path and molecular relaxation time. However, as shown in Section 10.2, the fluid density near the solid–liquid interface can vary significantly over intermolecular distances. While these local density oscillations may not necessarily mean the breakdown of the continuum theory, it is important to understand in detail how the continuum theory works for fluids in confined nanochannels.

During the last several years, researchers have used MD simulations to test the accuracy of Navier–Stokes equations in nanochannels (Koplik et al., 1989; Koplik et al., 1987; Travis and Evans, 1996; Travis et al., 1997; Bitsanis et al., 1987; Travis and Gubbins, 2000; Pozhar, 2000). In many of these simulations, a Poiseuille flow with a constant force on each fluid molecule is used as a prototypical problem. The continuum Navier–Stokes equations predict a parabolic velocity profile across the channel for the Poiseuille flow. The velocity profiles in slit channels as narrow as 10 molecular diameters indicate that the deviation between continuum and MD predictions is very small (Travis et al., 1997). Figure 10.13 shows the velocity profile obtained from MD simulation of Poiseuille flow in an 11-fluid-diameter channel and its quadratic fit. Clearly, the deviation of the velocity profile from the Navier–Stokes equation is small. However, if the channel width is smaller than 10 fluid diameters, the deviation of the MD velocity from the continuum prediction becomes more significant (Travis and Gubbins,

2000; Travis et al., 1997). For example, Figure 10.14 shows the velocity distribution for Poiseuille flow in a 4-fluid-molecule-diameter slit channel for three systems (see Section 10.2 for a description of the potentials used in the three systems) with different interaction potentials between fluid–wall and fluid–fluid (Travis and Gubbins, 2000). For each system considered, the velocity profile obtained from MD simulations is no longer parabolic and deviates significantly from the Navier–Stokes prediction. Specifically, for system A (we will discuss only the result for system A, since the results for system B and system C are similar to that of system A), the velocity decreases in the region $0.75 < |z| < 0.97$ as we approach the channel center, and there is a local maximum for the velocity located at $|z| \approx 0.95$. The corresponding strain rate profile is shown in Figure 10.15, and the strain rate is zero at $|z| \approx 0.97$ and $|z| \approx 0.2$. The fluid viscosity inside the channel, calculated by

$$\mu(z) = \frac{\tau_{xz}(z)}{\gamma(z)}, \tag{10.4}$$

is shown in Figure 10.16. Note that in equation (10.4), $\tau_{xz}(z)$ is the shear stress at position z, and a local, linear constitutive relationship between the shear stress and the strain rate, on which the classical Navier–Stokes equation is based, is assumed. We observe that the viscosity calculated by equation (10.4) is negative in the region $0.75 < |z| < 0.97$ and $0 < |z| < 0.2$ and diverges at $|z| \approx 0.97$ and $|z| \approx 0.2$. This indicates that the viscosity in such a narrow channel cannot be described by a local, linear constitutive relation. Therefore, the classical Navier-Stokes equation is not valid for the analysis of fluid flow in a 4.0-fluid-diameter slit channel.

For fluid flow in channels larger than 10 fluid molecular diameters, the classical Navier–Stokes equation can be used to analyze the flow. However, since the fluid can be highly confined in nanochannels, the fluid viscosity may be significantly different from the bulk value. Despite the fact that the fluid viscosity is an important parameter in determining the flow characteristics, only a few papers have discussed the viscosity of fluids in nanochannels systematically. (Bitsanis et al., 1990) have calculated the effective viscosity for Couette and Poiseuille flow in slit channels ranging from 2 to 9.5 fluid molecular diameters. The effective viscosity is defined in such a way that the Navier–Stokes equation using the effective viscosity can predict the macroscopic observables correctly, e.g., the surface shear stress in a Couette flow or the flowrate in a Poiseuille flow. Figure 10.17 shows the variation of the effective viscosity for Couette and Poiseuille flow with the pore width. The plot indicates that:

1. The effective fluid viscosity is flow-dependent;

2. At small pore width, the effective viscosity increases dramatically; and

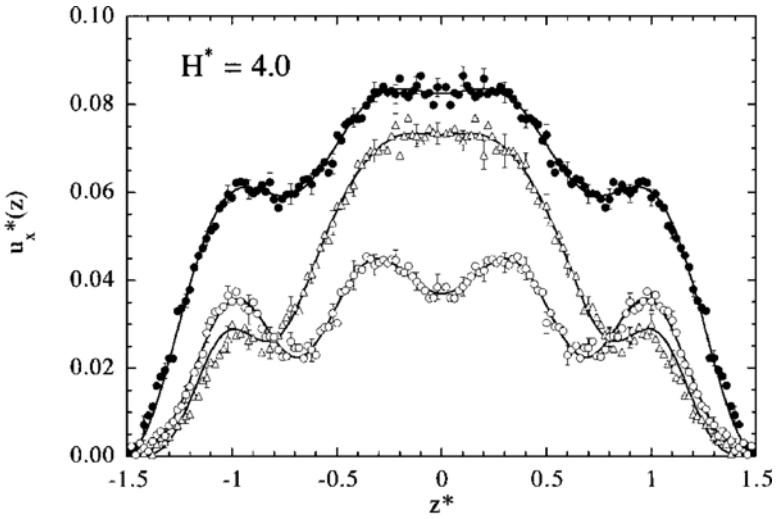

FIGURE 10.14. Velocity profiles in a 4.0-fluid-diameter slit channel for three different systems. System A: WCA system, filled circles; system B: LJ system, open circles and system; C: WCA-LJ system, open triangles. See Section 10.2 for the definition of the three systems. (Courtesy of K.P. Travis.)

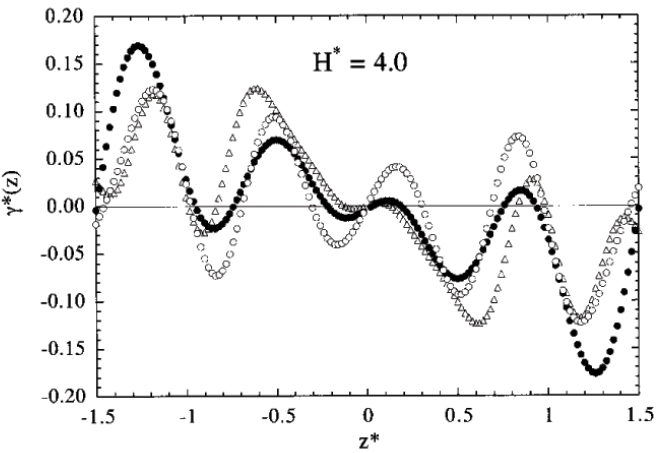

FIGURE 10.15. Strain rate profiles in a 4.0-fluid-diameter slit channel for three different systems. System A: WCA system, filled circles; system B: LJ system, open circles; and system C: WCA-LJ system, open triangles. (Courtesy of K.P. Travis.)

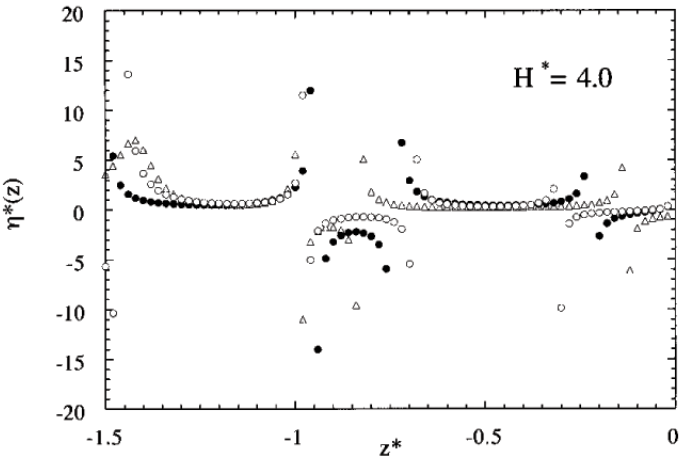

FIGURE 10.16. Shear viscosity in a 4.0-fluid-diameter slit channel for three different systems as calculated by equation (10.4). System A: WCA system, filled circles, system B: LJ system, open circles and system C: WCA-LJ system, open triangles. (Courtesy of K. P. Travis)

3. The effective viscosity converges toward the bulk viscosity as the pore width increases.

The first observation originates from the definition of the effective viscosity for the flow. The second observation is caused by the fluid layering near the pore surface. As the pore width decreases, more fluid molecules are observed within the fluid layers near the pore wall, where the movement of the fluid molecules is highly confined, thus leading to a higher effective viscosity.

Over the past decade, Pozhar has developed a rigorous statistical-mechanics approach to nonequilibrium phenomena in strongly inhomogeneous fluids (Pozhar, 1994; Pozhar, 2001; Pozhar, 2000). The approach relies on the rigorous generalization of the Mori–Zwanzig projection operator technique developed in the framework of the theory of dynamical systems. This approach, unlike the LADM method, has been realized for the most general case of strongly inhomogeneous fluids. However, due to the complicated nature of the theory, there have been very few applications of this method for the analysis of fluid flow. Therefore, the accuracy of the theory has not yet been rigorously established.

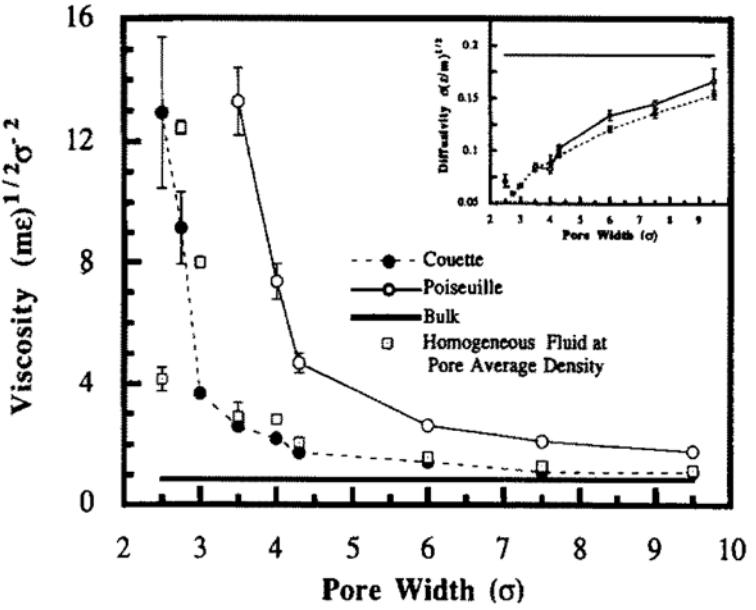

FIGURE 10.17. Effective viscosities for Couette and Poiseuille flows versus pore width. The viscosity of a homogeneous fluid at the pore average density is also shown. The inset shows the variation of the pore-averaged self-diffusion coefficients. (Courtesy of H.T. Davis.)

10.5 Boundary Conditions at Solid–Liquid Interfaces

In this section we revisit the question of slip at solid–liquid interfaces and present an in-depth review of the experimental work as well as the conceptual models derived from these findings. We then present different mathematical models that correct the no-slip condition and have been found to represent the available experimental data reasonably well.

10.5.1 Experimental and Computational Results

The first experimental work to investigate the validity of the no-slip boundary condition at a solid surface was conducted by Coulomb (1784), who concluded that it was valid even at microscopic scales. About a century later, Helmholtz and von Piotrowski (1860) found evidence of slip between a solid surface and a liquid, and later, (Brodman, 1891) verified their results. However, Couette (1890) and others used glass tubes with grease inside and concluded that the no-slip boundary condition is valid. It is

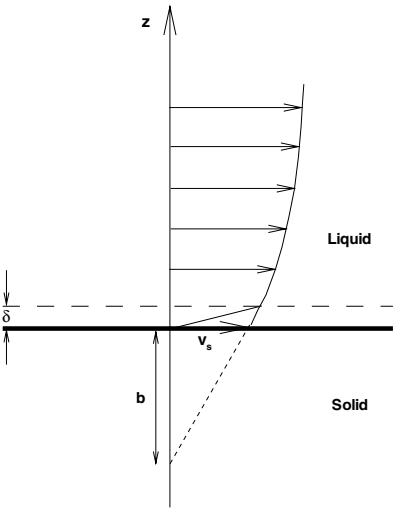

FIGURE 10.18. Definition of slip length b. The inner boundary layer δ is explained in the section on conceptual models of slip.

worth noting also that the experiments of Whetham (1890) that led to the acceptance of the no-slip condition were made on hydrophilic surfaces (Bonaccurso et al., 2003).

Navier (1823) was the first to model partial slip at the wall for liquids well before Maxwell's slip condition for gases (1879). Specifically, Navier's boundary condition at the wall is

$$\boldsymbol{v}_s = b\mathbf{n} \cdot \left(\nabla \boldsymbol{v} + \nabla^T \boldsymbol{v}\right). \tag{10.5}$$

An interpretation of the slip length b is shown in the sketch of Figure 10.18 for unidirectional flow over a flat wall. It is the distance behind the solid–liquid interface at which the velocity extrapolates to zero.

The validation of slip boundary conditions continued in the beginning of the twentieth century, focusing mostly on flow in capillaries. (Traube and Whang, 1928) reported a four- to five-fold increase in flowrate of water in a capillary treated with oleic acid. However, their results could be interpreted either as boundary slip or simply as surface-tension-induced capillary rise. In independent experiments with water flowing in capillaries treated with paraffin, (Ronceray, 1911) also studied how changes in the surface tension may affect the flowrate but concluded aganist the slip condition. The most systematic study, perhaps, of this effect was undertaken by (Schnell, 1956), who used water in glass capillaries (from 240 to of 800 μm) treated with dimethyldichlorosilane (i.e., silicone) to make them hydrophobic. He found that for a small pressure drop in the capillary the flowrate was lower in

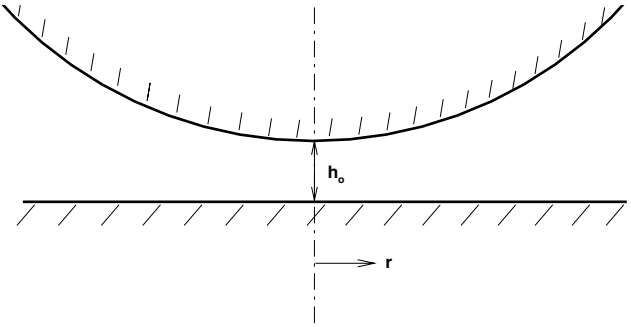

FIGURE 10.19. Schematic of the surface force apparatus (SFA).

the treated cases compared to the untreated ones, but at higher pressure drop he observed the opposite. Interestingly, at velocities past the onset of turbulence there was no discerible difference in flowrate. Overall, Schnell's experiments stood the test of time and are considered the first to prove convincingly that a boundary slip occurs for hydrophobic (i.e., water-repellent) surfaces. This result agrees with the physical intuition, i.e., that boundary slip is larger in hydrophobic surfaces, since the attractive forces between the liquid and the solid surface are less than for hydrophilic surfaces, and thus the solid–liquid interface friction is reduced. At about the same time, it was established by (Debye and Cleland, 1959) that boundary slip can also occur in liquid hydrocarbons for flow through porous Vycor glass.

In the last few decades there has been a renewed interest in determining the validity of the no-slip boundary condition for liquids due to the interest in polymers and other complex fluids but primarily due to microfluidic applications. In (Chuarev et al., 1984), both water and mercury were tested in flow through glass capillaries of diameter less than 10 μm treated with trimethylchlorosilane. It was found that for water with contact angles less than 70° the no-slip condition was valid, but for higher hydrophobicity increased flowrates were obtained corresponding to a slip length between 30 and 200 nm according to Navier's formula of equation (10.5). For mercury, a contact angle of more than 130° also led to boundary slip. These results suffer, however, from the limitation in determining the capillary diameter precisely as well as in controlling the homogeneity of the internal capillary surface.

The effective use of the surface force apparatus (SFA) in the 1990s has led to many interesting experimental results and detailed studies of boundary slip with water and other substances. SFA employs a sphere in close proximity to a plane, but other configurations are also possible, e.g., two crossed cylinders. The two surfaces are approaching at a controlled speed, causing drainage of the liquid placed within the sphere–plane gap; see sketch of figure 10.19. Typically, an oscillation of small amplitude is imposed on the sphere (or the plane), and the response force on the plane is recorded. The

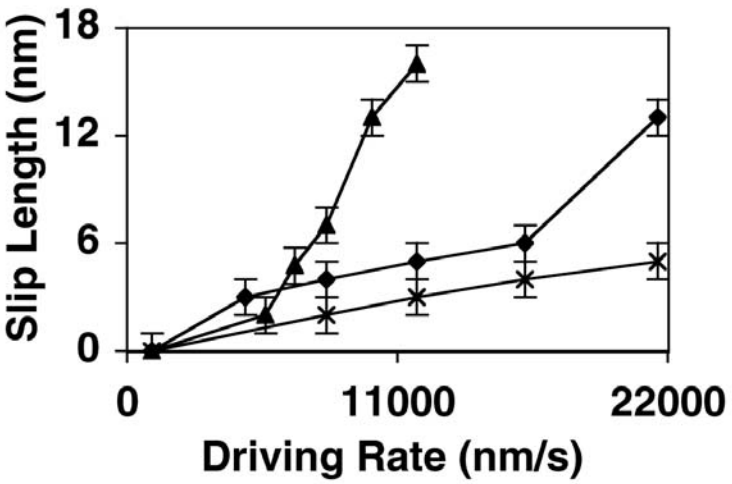

FIGURE 10.20. Slip length versus driving rate obtained in SFA experiments. Sucrose solutions of different concentrations are used to change the viscosity: 19.2 mPa s (crosses); 38.9 mPa s (diamonds); 80.3 mPa s (triangles); taken from (Craig et al., 2001). (Courtesy of V. Craig.)

ratio of the force component in-phase with the oscillation to the amplitude of the oscillation gives the normal stiffness coefficient, while the corresponding ratio for the out-of-phase component gives the damping coefficient.

In (Baudry et al., 2001), a drop of glycerol was placed between the two surfaces with roughness of about 1 nm. The surfaces of the plane and the sphere were coated with thiol and gold, respectively, in a first set of experiments, and with thin cobalt film (for both sphere and plane) in a second set of experiments; cobalt makes the surface hydrophilic, while thiol makes it hydrophobic. The measured (advancing) contact angles for thiol and cobalt were 94° and 62°, respectively. The main finding, based on the measured damping coefficient, was that at sphere–plane distances less than 300 nm the hydrophobic surface gave a large deviation from the no-slip condition with slip length $b \approx 40$ nm, while for the cobalt surface the slip was zero. The molecular size of the glycerol molecule is 0.6 nm, so the slip length is about 65 times the molecular diamater of glycerol. Interestingly, at distances smaller than 5 nm, both hydrophobic and hydroplilic surfaces gave the same response and it was assumed that at these small distances the film did not behave like a liquid.

In (Craig et al., 2001), SFA measurements were also used to infer boundary slip for water on sphere–plane surfaces with (advancing) contact angle 70°. The silica sphere and the mica flat surface were coated with a layer of gold and an additional layer of titanium to promote adhesion. Aqueous solutions of sucrose at various concentration levels were used to control the

viscosity magnitude. It was found that at low viscosity and low approach rate of the surfaces, the no-slip condition was valid, whereas at higher viscosities and shear rates boundary slip was observed. The corresponding slip length was up to 18 nm, corresponding to the highest viscosity of the aqueous solutions (80.3 mPa s) and varied nonlinearly with the driving rate (up to 22 μm/s). A summary of these results is included in Figure 10.20. In a follow-up experiment in (Bonaccurso et al., 2003), the effect of roughness mounted on hydrophilic surfaces on the slip length was investigated. Roughness with rms heights of 0.7 nm, 4 nm, and 12.2 nm was tested, and the force curves showed clearly an enhanced slip at the wall as the roughness increased. The particular slip length value depended on the way that the data were fitted, but very large values of b were reported on the order of *hundreds of* nanometers.

In (Zhu and Granick, 2001), SFA measurements with molecularly smooth surfaces of mica were obtained for water (polar) and tetradecane (non polar), an oil with low viscosity close to water. In particular, three different liquid–solid systems were considered with increasing contact angle: (1) tetradecane against adsorbed surfactant; (2) tetradecane against a methyl-terminated self-assembled monolayer (SAM), and (3) water against a methyl-terminated SAM. In the last two cases a monolayer of octadecyltriethoxysiloxane (OTE) was used on which the (advancing) contact angle of water was 110° and that of tetradecane was 44°. It was found that for cases (2) and (3) with the OTE layer causing partial wetting of the surface, boundary slip was obtained for film thickness less than about 100 μm. However, case (1) gave no slip at the solid interface. The results of (Zhu and Granick, 2001) led to similar conclusions as in (Craig et al., 2001), in that the slip length depends strongly on the approach (driving) rate and is largest for water: the largest value is $b \approx 35$ nm at shear rates about 10^3 s^{-1}. Below a threshold value of the approach rate (and thus shear rate) the no-slip boundary condition is valid.

The effect of roughness on boundary slip was examined in a follow-up paper by the same researchers (Zhu and Granick, 2002). Roughnesses with rms values up to 6 nm were fabricated using self-assembled OTE monolayers and OTS (octadecyltrichlorosilane) layers. The advancing contact angle was similar for all cases, but the receding contact angle was a decreasing function of surface roughness. It was hypothesized that large roughness will *decrease* the slip length, although cases with an increase in slip length have also been reported (Bonaccurso et al., 2003; Ponomarev and Meyerovich, 2003). The results of (Zhu and Granick, 2002) are summarized in Figure 10.21, where atomic force microscopy images of roughness on a $3\,\mu\text{m} \times 3\,\mu\text{m}$ area are also shown. The data of (Zhu and Granick, 2002) show that even the case of largest slip length ($b \approx 35$ nm) for water produces no slip at the wall if the roughness rms height exceeds 6-nm. The critical shear rate for onset of slip seems to depend linearly on the roughness *rms* height and is independent of its wavelength. For 6-nm roughness a value of shear rate

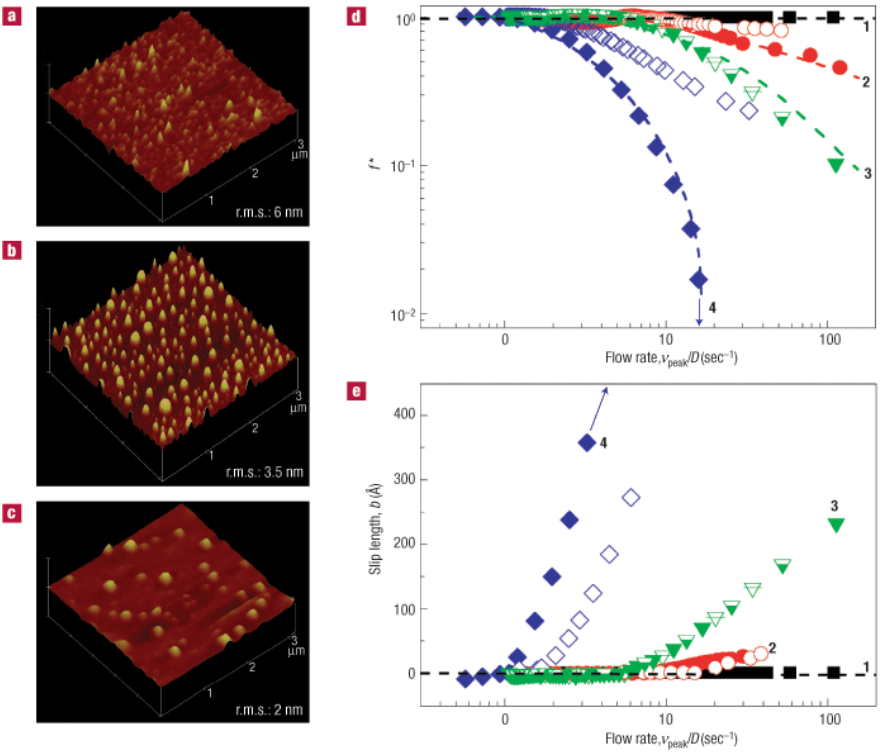

FIGURE 10.21. Effect of roughness and flow rate (or driving rate) on boundary slip. Plots (a), (b) and (c) show images of roughness at 6 nm, 3.5 nm, and 2 nm, respectively. Plot (d) shows the correction factor in the Reynolds–Vinogradova theory (equation (10.11)), and plot (e) the corresponding slip length. Filled symbols correspond to *deionized water* and open symbols to *tetradecane*. The various curves correspond to roughness of: squares - 6 nm; circles - 3.5 nm; triangles - 2 nm; and diamonds – atomically smooth. (Courtesy of S. Granick.)

of 10^5 s^{-1} is required to cause onset of boundary slip. These results are in disagreement with the results of (Bonaccurso et al., 2003) for hydrophilic surfaces.

There has been some skepticism regarding the findings of boundary slip based on the SFA measurements. However, similar conclusions were obtained in (Bonaccurso et al., 2002), using a colloidal probe technique to measure forces between hydrophilic surfaces (mica and glass) for water. In particular, spherical borosilicate glass particles of radius 10 μm were sintered to atomic force microscope (AFM) cantilevers. The hydrophilic surface was periodically moved up and down, and the cantilever deflection was measured optically. A slip length of up to 9 nm was measured for shear

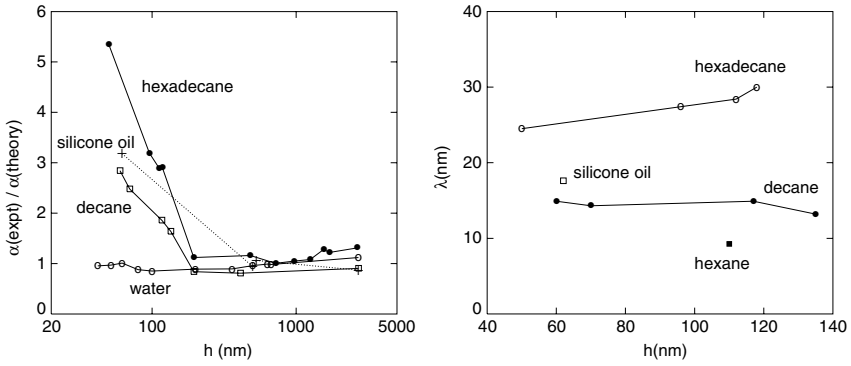

FIGURE 10.22. Normalized flowrate (left) and slip length versus channel height for several fluids. (Courtesy of N. Giordano.)

rates of 10^4 s^{-1}. Electrokinetic effects, which could render the data erroneous by causing an increase of the effective viscosity in the electric double layer (EDL), were found insignificant. In another study in (Pit et al., 2000), a novel technique was employed to test boundary slip for hexadecane flowing over a hydrocarbon/lyophobic smooth surface. This technique was adapted from an experimental setup used to investigate boundary slip in polymers. In particular, fluorescent probes of the size of the hexadecane molecules were used as traces in a capillary formed between two parallel disks, only one of which was rotating. A combination of fluorescence recovery after photobleaching and total internal reflection at the solid–liquid interface was employed to directly probe the velocity within 80 nm of a solid wall. The surface was made of modified sapphire treated with OTS ($\gamma > 21$ mJ/m^2) and FDS (perfluorodecanetrichlorosilane, $\gamma < 13$ mJ/m^2) in order to change the interfacial energy in a controlled manner. It was found that for the bare sapphire surface a slip length of 175 nm ($\pm$50 nm) was obtained, while for a dense OTS layer the slip length was 400 nm ($\pm$100 nm) independent of the shear rate in the range from 200 s^{-1} to 2000 s^{-1}. For the FDS surface no boundary slip was observed. In agreement with most of the other investigators, (Pit et al., 2000) also hypothesized that roughness decreases slip, and thus it is in competition with the strength of the fluid–surface interaction.

With regard to microfluidic applications directly involving microchannels, it is not clear how much the slip boundary condition depends on the way that the flow is driven, although the majority of the experimental work clearly points to a strong dependence on the shear rate (an exception is the work of (Pit et al., 2000)). In the work of Bau and collaborators (Urbanek et al., 1993), a pressure-driven flow was considered, and boundary slip was reported for channels with the smallest height of 20 μm and

silicone oil as well as isopropol alcohol (see Figure 1.16 in Section 1.2). A comprehensive study of pressure-driven flows was undertaken in (Cheng and Giordano, 2002), with several fluids for very small microchannels fabricated lithographically down to 40 nm. The channel width was 20 μm, and the length was in the range of 100 to 900 μm; the roughness was about 0.5 nm. The flowrate was measured using a macroscopic capillary in series with the outlet side of the sample, but for smaller flowrate values a microchannel was fabricated and the flow was measured with photomicroscopy. One of the surfaces of the channel was glass, and the other one was coated with photoresist; no measurements of the contact angle were made.

In Figure 10.22 (left) the flowrate normalized by the theoretical prediction for no-slip Poiseuille flow is plotted, taken from (Cheng and Giordano, 2002). Specifically,

$$\alpha_{\text{theory}} = \frac{h^3 w}{12 \mu L}$$

(where h, w, L denote the height, width, and length of the microchannel) is used in the normalization. We see that for all the liquids tested, the flowrate increases except for water. In particular, hexadecane (the fluid with the largest molecular size) exhibits the largest deviation from the no-slip theory. This is in agreement with the results in (Pit et al., 2000), for the capillary hexadecane flow, although the slip length values reported in (Cheng and Giordano, 2002), are much smaller. In general, the experimental evidence given in (Cheng and Giordano, 2002), indicates a monotonic increase of the slip length with the molecular size but for channel height $h < 300$ nm; above this value the no-slip theory seems to be valid according to the results of (Cheng and Giordano, 2002). This dependence on the molecular structure is shown in Figure 10.22 (right), indicating also that there is some weak dependence of the slip length on the channel height in the slip regime. However, this effect may be associated with the uncertainties in measuring the very small values of h.

Other experiments with larger microchannels for pressure-driven flows revealed boundary slip for water, in contrast to the aforementioned results of (Cheng and Giordano, 2002). For example, in (Tretheway and Meinhart, 2002), microPIV (300-nm diameter fluorescent polystyrene spheres) was used to measure velocity profiles of water in a $30 \times 300\,\mu$m channel. The channel surfaces were treated with a 2.3 nm OTS layer. The velocity profiles were measured in a $25 \times 100\,\mu$m plane to within 450 nm of the channel wall. A slip velocity of about 10% of the maximum velocity was measured, which corresponds to slip length of about 1 μm. This is a very large value for the slip length, of the order of magnitude that is typically encountered in polymer flows. For the untreated glass surface, which is hydrophilic, no-slip conditions were observed. Similar reults were also reported in (Choi et al., 2003), in smaller hydrophobic microchannels of 0.5 μm and 1 μm height. The channels were 500 μm wide and 9 mm long, while the sur-

faces were coated with OTS layers to make them hydrophobic. In both the experiments of (Tretheway and Meinhart, 2002) and (Choi et al., 2003), roughness was negligible. The slip length was found to depend linearly on the shear rate with $b = 30$ nm at a shear rate of 10^5 s^{-1} for hydrophobic surfaces, while for hydrophilic surfaces $b = 5$ nm at the same shear rate. The corresponding slip velocity was of order 3 mm/s for the hydrophobic case and 0.5 mm/s for the hydrophilic case.

In *MD simulations* the slip length predicted is typically much lower due to the substantial pressure imposed, which can modify the wetting properties of the surface. Specifically, MD simulations with hexadecane were performed in (Stevens et al., 1997), and dependence on the strength of the liquid–wall interaction was established similar to that in the experiments. However, a realistic representation of the surface, i.e., to account accurately for the glass or sapphire or other surfaces tested experimentally, is not available. In (Cieplak et al., 2001), MD simulations were performed for a simple molecule as well as a chainlike molecule. They were described by a shifted Lennard–Jones potential for two atoms for the former and for ten atoms for the latter. The consecutive atoms along the chain were tethered by the finitely extensible nonlinear elastic potential (FENE) used often in polymer modeling; it has the form

$$V_{\mathrm{FENE}} = -\kappa/2r_0^2 \log[1 - (r/r_0)^2], \tag{10.6}$$

where $\kappa = 30\epsilon$ and $r_0 = 1.5\sigma$. The crucial wall–fluid interaction was modeled by a distinct Lennard–Jones potential of the form

$$V_w = 16\epsilon[(r/\sigma)^{-12} - c_{\mathrm{FS}}(r/\sigma)^{-6}],$$

where c_{FS} determines the wall type, so that $c_{\mathrm{FS}} = 1$ corresponds to a thermal (attractive) wall and $c_{\mathrm{FS}} = 0$ corresponds to a specular (repulsive) wall. The narrowest channel simulated had dimensions of $13.6\sigma \times 5.1\sigma \times 12.75\sigma$, with the the last dimension denoting the distance between the two walls (channel height).

The results for Couette flow in (Cieplak et al., 2001), suggest that the slip length is independent of the type of flow or the channel height, but that it is a strong function of the wall type. When $c_{\mathrm{FS}} = 0$ there is a relatively large slip (about 10σ), but for $c_{\mathrm{FS}} = 1$ the slip length is equal to the negative of the distance between the wall and the second layer (about -1.7σ). In the case of a chain molecule, the slip length depends more strongly on the value of c_{FS}, and for $c_{\mathrm{FS}} = 1/4$ the slip length is 20.6σ, in qualitative agreement with the MD simulation results of (Stevens et al., 1997) for hexadecane and also with the experimental results of (Pit et al., 2000).

Similar results were reported in (Priezjev and Troian, 2004), for shear polymer films in a Couette flow with a gap height of 24.57σ. In particular, N-mer polymer chains with N up to 16 were simulated for various levels of shear rate $\dot{\gamma}$. The scaling law obtained in the earlier simulations of

(Thompson and Troian, 1997) for $N = 1$, see equation (1.2), was extended for polymer chains; that is, the normalized slip length is given by

$$\frac{b}{b_s^0} = \left(1 - \frac{\dot{\gamma}}{\dot{\gamma}_c}\right)^{-1/2} \tag{10.7}$$

for shear rates $\gamma \geq 5 \times 10^{-3}\tau^{-1}$; γ_c is the critical level of shear rate above which divergence behavior is observed. It was also found that beyond $N = 10$ the molecular weight dependence of the slip length is mostly associated with the bulk viscosity.

Also, in (Barrat and Bocquet, 1999), MD simulations were performed with a Lennard–Jones potential of the form

$$V_{\mathrm{LJ}} = 4\epsilon[(r/\sigma)^{-12} - c_{ij}(r/\sigma)^{-6}],$$

where c_{ij} controls the type of interaction. The interactions between fluid atoms were defined by $c_{\mathrm{FF}} = 1.2$, while the fluid–solid interaction coefficient c_{FS} was varied between 0.5 and 1. For $c_{\mathrm{FS}} = 0.9$ a contact angle of 100° is obtained, whereas for $c_{\mathrm{FS}} = 0.5$ a contact angle of 150° is obtained, which is close to the case of mercury on a glass surface, a flow configuration studied in the experiments of (Chuarev et al., 1984) with mercury flowing through glass capillaries. For this hydrophobic case a slip length of about 15 molecules was computed, whereas for the 100° case the no-slip condition was valid all the way to the wall boundary. Taking into account that the molecule size is about 0.25 nm, the maximum computed slip length in the MD simulations of (Barrat and Bocquet, 1999) is about 4 nm, which is still much smaller than any of the experimental data, especially for hydrophobic surfaces.

10.5.2 Conceptual Models of Slip

We have seen that the MD simulations systematically underpredict the slip length deduced from the various experiments either based on force curves in the surface force apparatus or based on the flowrate measured in capillaries and microchannels. Specifically, the MD simulations predict a slip length roughly *ten times smaller* than in the experiments, and such a large discrepancy implies that there are some other physical phenomena not included in the simulation. Here we present some of the physical models that have been proposed in the literature that can justify the large values of slip length and the origin of slippage.

1. Molecular slippage: This theory first appeared in the Russian literature and is due to Tolstoi (1952); it was analyzed more thoroughly in (Blake, 1990). It provides a link between the mobility of the molecules in the first few layers closer to the wall with the interfacial energy associated with the liquid–solid interface. Therefore, it relates directly the contact angle to the slip length.

2. Gaseous film: This model was first suggested by (Ruckenstein and Rajora, 1983) and was also discussed by (Vinogradova, 1999). It assumes that there may be a film of gas at the interface between the solid surface and the liquid. The origin of this film may be due to external dissolved gases up to metastable concentrations. According to (deGennes, 2002), this gas film nucleates bubbles preferentially near the wall at contact angles greater than 90°, i.e., on hydrophobic surfaces. This mechanism can take place above a threshold in shear rate, a fact consistent with the experimental observations. Evidence of nanobubbles on a hydrophobic glass surface in water using an atomic force microscope was reported in (Tyrrell and Attard, 2002). Another possibility, consistent with MD simulations that reveal a depletion of the first layer of molecules, is that a flat vapor bubble is generated at the solid–liquid interface due to thermal fluctuations. In either case, the gaseous film is assumed to be small, e.g., less than 0.5 nm.

A simple mathematical model was proposed by (deGennes, 2002) for this case. He assumed that the gas in the gap is in the molecular regime (since the mean free path satisfies $\lambda \gg h$, where h is the film thickness), and thus the only collisions are with the wall. Correspondingly, a molecule leaving the liquid has a Gaussian velocity distribution for the tangential velocity component with the corresponding peak at the slip velocity v_s. Denoting by ρ, m the density and molecular mass of the gas, respectively, the average momentum transmitted to the solid by the gas is mv_s, and thus the shear stress σ at the wall is

$$\sigma = mv_s \frac{\rho}{m} \bar{v}_y = \rho v_s \bar{v}_z,$$

where $(\rho/m)\bar{v}_z$ is the average number of collisions with the wall, and the normal to the surface average velocity $\bar{v}_z$ is

$$\bar{v}_z = \frac{v_{th}}{\sqrt{2\pi}} \quad \text{with} \quad v_{th} = \sqrt{kT/m}.$$

On the other hand, $\sigma = \mu \partial v/\partial z = \mu v_s/b$, and thus by comparing with the above expression, we obtain the slip length

$$b = -h + \frac{\mu}{\rho \bar{v}_z} \approx \frac{\mu}{\rho \bar{v}_z},$$

where the thickness h of the gaseous film is assumed negligible. Upon substitution of typical values for water vapor in the above expression, we obtain a slip length of a few microns, which is clearly much higher than any of the available experimental data. We note that the model of de Gennes shows that the slip length increases with the viscosity and thus with the molecular weight, which is consistent with the measurements in (Cheng and Giordano, 2002).

3. Viscosity model: This model, proposed by (Vinogradova, 1999), is inspired by the slip mechanism in polymer melts. It provides a connection between the slip length and a decrease in viscosity within a very thin

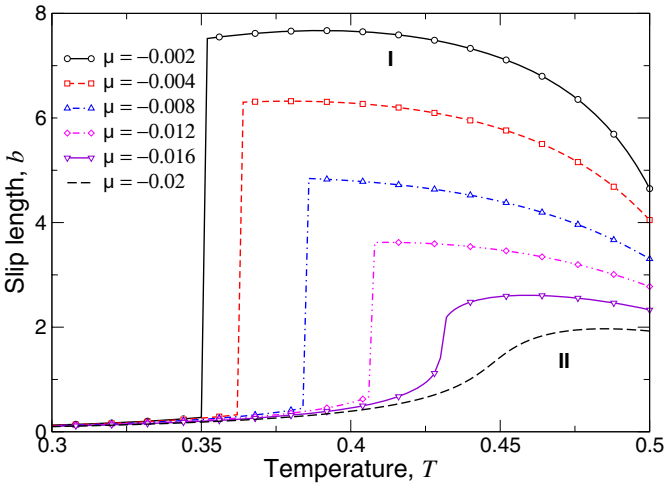

FIGURE 10.23. Slip length versus temperature in prewetting transition for different values of the chemical potential μ. (Courtesy of O.I. Vinogradova.)

boundary layer δ close to a hydrophobic surface. Assuming a *bulk viscosity* μ_b and a *near-wall viscosity* μ_s, then the slip length is

$$b = \delta \left(\frac{\mu_b}{\mu_s} - 1 \right).$$

This expression shows that there are two mechanisms for obtaining a large slip length, i.e., either by increasing δ or by increasing the viscosity ratio in the bulk and the surface. For example, for $\mu_b/\mu_s = 21$ and $\delta = 10$ nm, a slip length of $b = 200$ nm can be obtained, but a more realistic viscosity ratio is $\mu_b/\mu_s = 3$, which corresponds to $b = 20$ nm.

The above arguments suggest that there may be another mechanism in place that produces thick films (i.e., large δ), and that is why in some experiments large values of the slip length have been reported. To this end, in (Andrienko et al., 2003), a new model that accounts for prewetting transition was developed. It takes into consideration the structure of the binary mixture in the region near the solid surface and allows for a temperature dependence of the thickness in the form $\delta \propto -\ln(|T_w - T|)$, where T_w is the wetting temperature of the surface.

The governing equation for this case is obtained in terms of the *order parameter* Φ, which is defined as

$$\Phi = \frac{n_1 - n_2}{n_1 + n_2},$$

where n_i denotes the number density of each species. This order parameter changes very fast very close to the interface, but it is almost constant in the bulk. The viscosity of the binary mixture can then be expressed as a

linear combination of its two components, i.e.,

$$\mu_m(z) = \mu_s \frac{1+\Phi(z)}{2} + \mu_b \frac{1-\Phi(z)}{2}.$$

The thermodynamics of the binary mixture are described via a free-energy functional plus other contributions to account for surface effects. The corresponding *semigrand potential* proposed in (Andrienko et al., 2003), is given by

$$U(\Phi) = \frac{1}{\sigma^3} \int dV \left(\frac{k}{2}\sigma^2 (\nabla\Phi)^2 + f(\Phi) - \mu\Phi \right) + \Psi_s,$$

where σ is a length scale characteristic of the molecule size, $f(\Phi)$ is the Helmholtz free-energy density, Ψ_s is the surface energy, and μ is the chemical potential. The governing equation is then obtained by minimizing the above functional to obtain

$$k\frac{\partial^2\Phi}{\partial z^2} + \frac{\Phi}{2} - \frac{1}{2}T \ln \frac{1+\Phi}{1-\Phi} + \mu = 0, \tag{10.8}$$

where T is the temperature. This is a boundary value problem, which was solved in (Andrienko et al., 2003), for a channel with identical walls located sufficiently far from each other so that the film layers do not overlap. The solution of the above equation reveals a *prewetting transition* that depends on the temperature; it is sudden, and it jumps from a thin film to a thick film (first-order transition). For thin films a small slip length is obtained, but for thick films a large slip length is obtained that also depends on the chemical potential. This is shown in Figure 10.23, which is taken from (Andrienko et al., 2003), and is in nondimensional units (the molecular size σ is employed in the nondimensionalization). When a thick film is obtained the corresponding slip length depends on temperature, while below the threshold for transition the slip length is independent of the temperature.

4. No-shear/no-slip patterning: This model was first considered in (Philip, 1972), in an attempt to explain slip in porous media. The main idea is to consider the liquid–solid interface segmented into aternating stripes of *no-slip* and *no-shear* and deduce an effective slip length from this static configuration. This model was advannced more recently by (Lauga and Stone, 2003) who extended some of the exact solutions in (Philip, 1972), and hypothesized the existence of small bubbles attached to the wall as providers of the slip and thus the corresponding *stress-free* condition. As was already mentioned, there is direct experimental evidence by AFM of the existence of such nanobubbles; see, for example, (Tyrrell and Attard, 2002). In rough surfaces or surfaces with tiny cracks, air pockets may exist that act as stress-free local boundaries. Therefore, the proposed model is that of surface heterogeneities that lead to an effective or equivalent macroscopic slip.

The two basic configurations, a *longitudinal* and a *transverse* one, considered in the works of (Philip, 1972) and (Lauga and Stone, 2003), are

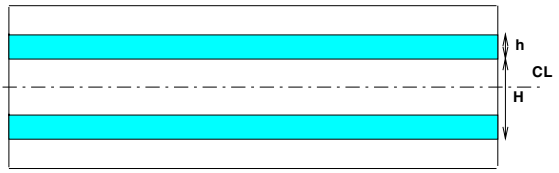

(a)

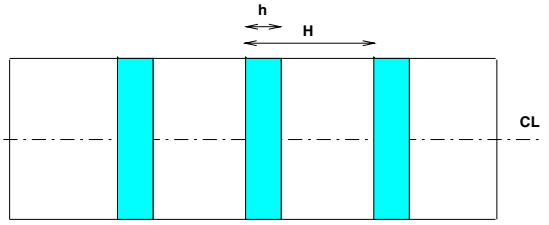

(b)

FIGURE 10.24. Longitudinal (a) and transverse (b) models of no-shear stripes.

shown in the sketch of Figure 10.24 for a capillary. Semianalytical Stokes flow solutions can be obtained for these geometries, and the effective slip length b_e can be obtained in terms of the ratios $\delta = h/H$ and $L = H/R$ and the capillary radius R. This effective slip length is defined indirectly from the flow rate as follows: Let us assume that the partial slip condition is applied everywhere, then the velocity profile is

$$u(r) = \frac{1 - r^2}{4} + \frac{b}{2R},$$

and correspondingly the nondimensional flowrate is

$$Q = \frac{\pi}{8}\left(1 + \frac{4b}{R}\right).$$

Solving for the effective slip length, we obtain

$$b = \frac{R}{4}\left(\frac{8Q}{\pi} - 1\right).$$

Therefore, by obtaining the flowrate for a given configuration, we can then obtain the effective slip length from above (Lauga and Stone, 2003).

For the *longitudinal* configuration, (with m no-shear bands with half-angle α) shown in Figure 10.24, an exact solution was obtained in (Philip, 1972) for the velocity distribution

$$u(r,\theta) = -\frac{R^2}{4\mu}\frac{\partial p}{\partial r}\left[1 - (r/R)^2 + (4/m)\Im\left(\cos^{-1}\left(\frac{\cos(M)}{\cos(m\alpha/2)}\right) - M\right)\right],$$

where $M = -im/2 \ln(re^{i\theta}/R)$ and $\Im$ implies imaginary part. The corresponding effective slip length, b_l, for this case is

$$\frac{b_l}{R} = \frac{2}{m} \ln\left(\sec(m\alpha/2)\right) = \frac{L}{\pi} \ln\left(\sec(\delta\pi/2)\right).$$

For the configuration with the *transverse* no-shear stripes the solution is a bit more complicated, but four asymptotic limits were obtained for the slip length b_t in (Lauga and Stone, 2003), in terms of the slip percentage δ and the separation between slip stripes L, as follows:

1. $b_t/R \propto \delta/4$ for $\delta \to 0$ and L fixed.
2. $b_t/R \propto [4(1-\delta)]^{-1}$ for $\delta \to 1$ and L fixed.
3. $b_t/R \propto (L/(2\pi)) \ln\left(\sec(\delta\pi/2)\right)$ for $L \to 0$ and δ fixed.
4. $b_t/R \propto [4(1-\delta)/\delta]^{-1}$ for $L \to \infty$ and δ fixed.

For a small percentage of slip, the above limits suggest that the effective slip length decreases faster (quadratically) to zero for longitudinal stripes compared to linear decrease for transverse slip stripes. For a large percentage of slip the opposite is true. Also, for small separation between slip stripes ($L \to 0$) we have that $b_l = 2b_t$. These two configurations represent the two extreme idealized cases, since in reality we expect a random distribution of no-shear pockets mixed with no-slip pockets. In addition, the dependence of the slip length of the shear rate can also be included in this model by assuming that the inhomogeneities (e.g., nanobubbles) are elongated at large values of shear rate, hence effectively increasing the relative no-shear to no-slip regions.

10.5.3 Reynolds–Vinogradova Theory for Hydrophobic Surfaces

In this section, we derive analytical solutions for the steady-state flow between two curved hydrophobic surfaces following the work of (Vinogradova, 1995; Vinogradova, 1996). This theory is an extension of Reynolds lubrication theory appropriate for *slip* surfaces.

The theory is valid for general curved surfaces, but for simplicity here we show the main steps in the solution for two spherical rigid bodies of radii R_1 and R_2. The distance h between the two bodies is small compared to the radii, and contact is allowed only at a single point. We also assume that a hydrophilic surface is characterized by $b = 0$. A schematic of the setup is shown in Figure 10.25; a cylindrical coordinate system is employed in deriving the solution. The relative velocity is $v = |v_1 - v_2|$, where the spheres move along the line connecting their centers with velocities v_1 and v_2.

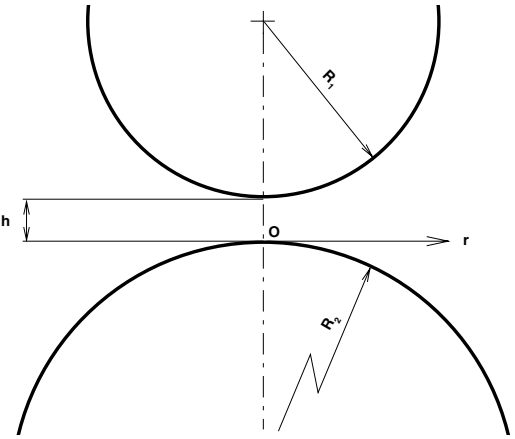

FIGURE 10.25. Geometry and notation for two spheres approaching each other.

The surfaces of the two bodies (upper and lower, respectively) can be described by paraboloid of revolution, i.e.,

$$Z = h + \frac{1}{2}\frac{r^2}{R_1} + \mathcal{O}(r^4) \quad \text{and} \quad Z = -\frac{1}{2}\frac{r^2}{R_2} + \mathcal{O}(r^4),$$

and introducing a shifted coordinate $z = Z + r^2/(2R_2)$ and $R_e = R_1 R_2/(R_1 + R_2)$, we can represent the two surfaces in a new coordinate system as

$$z = h + \frac{1}{2}\frac{r^2}{R_e} + \mathcal{O}(r^4) \quad \text{and} \quad z = \mathcal{O}(r^4).$$

The governing equation is Reynolds's lubrication equation, assuming that the characteristic length is the gap between the two particles, i.e.,

$$\mu \frac{\partial^2 v_r}{\partial z^2} = \frac{\partial p}{\partial r},$$

while in the z-direction we have that $\partial p/\partial z = 0$, which implies that the pressure is a function of r only. The boundary conditions correspond to slip on the lower body, characterized by $b_2 = b$, while on the upper surface we assume that $b_1 = b(1 + k)$, where k characterizes the specific type of the interaction. Specifically,

- $k = -1$ corresponds to a hydrophilic upper surface.
- $k = 0$ corresponds to a hydrophobic upper surface.
- $k \to \infty$ corresponds to a bubble upper surface.

In addition, k can take any other value between -1 and ∞ to represent other types of interaction and surfaces. We note that contrast to the standard Reynolds problem, where the only length scale present is the gap h,

here we have two additional length scales, namely b and $b(1+k)$. So the boundary conditions on the lower surface are

$$v_z = 0 \quad \text{and} \quad v_r = b\frac{\partial v_r}{\partial z}$$

and those on the upper surface are

$$v_z - \frac{rv_r}{R_e} = -v \quad \text{and} \quad v_r = -b(1+k)\frac{\partial v_r}{\partial z}.$$

The solution of the above Reynolds equation with the aforementioned boundary conditions yields

$$v_r(r,z) = \frac{1}{2\mu}\frac{\partial p}{\partial r}\left[z^2 - z\frac{H(H+2b(1+k))}{H+b(2+k)} - \frac{bH(H+2b(1+k))}{H+b(2+k)}\right],$$

where $H = h + r^2/(2R_e)$. The relative velocity v can be obtained from the continuity equation

$$\frac{\partial v_z}{\partial z} + \frac{1}{r}\frac{\partial (rv_r)}{\partial r} = 0,$$

which by integration yields

$$v = \frac{1}{r}\frac{\partial}{\partial r}\left[(r\frac{\partial p}{\partial r})\frac{1}{2\mu}\left(\frac{H^3}{3} - \frac{H^3(H+2b(1+k))}{2(H+b(2+k))} - \frac{bH^2(H+2b(1+k))}{H+b(2+k)}\right)\right].$$

This velocity is constant, and thus we can solve the above differential equation in terms of pressure by integrating twice and assuming that $p = 0$ at $r \to \infty$, and $\partial p/\partial r = 0$ at $r = 0$ due to symmetry. The equation for the pressure is then

$$p(r) = -\frac{3\mu R_e v}{H^2}p^*, \tag{10.9}$$

consisting of two factors, namely, the Reynolds part and the correction factor p^* given by

$$p^* = \frac{2AH}{BC} + \frac{2H^2}{C-B}\left(\frac{B-A}{B^2}\ln(1+B/H) - \frac{C-A}{C^2}\ln(1+C/H)\right). \tag{10.10}$$

The constants A, B, C in this expression characterize the two surfaces; they are given by

$$\begin{aligned} A &= b(2+k), \\ B &= 2b(2+k+\sqrt{1+k+k^2}), \\ C &= 2b(2+k-\sqrt{1+k+k^2}). \end{aligned}$$

The resistance forces acting on the spheres are equal in magnitude and are primarily due to the pressure, so the force can be computed exactly from $F_z = \int_0^\infty p2\pi r dr$, to obtain

$$F_z = -\frac{6\pi\mu R_e^2 v}{h}f^*, \tag{10.11}$$

s

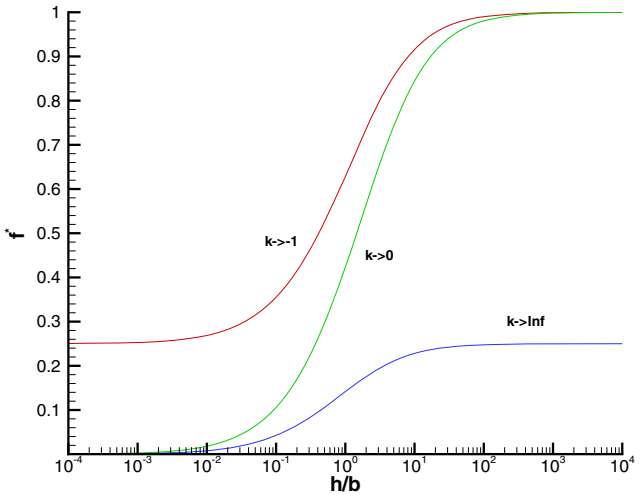

FIGURE 10.26. Correction factor f^* as a function of the gap to slip length ratio for the three asymptotic cases discussed in the text.

consisting also of two factors, namely, the Reynolds part and the correction factor f^* given by

$$f^* = -\frac{Ah}{BC} - \frac{2h}{C-B}\left(\frac{(B+h)(B-A)}{B^2}\ln(1+B/h) - \frac{(C+h)(C-A)}{C^2}\ln(1+C/h)\right). \tag{10.12}$$

For the aforementioned three limiting cases, the above expression reduces to

$$f^* = \frac{1}{4}(1+\frac{3h}{2b}\left[(1+h/(4b))\ln(1+4b/h)-1\right] \quad \text{for } k=-1,$$
$$f^* = \frac{h}{3b}\left[(1+h/(6b))\ln(1+6b/h)-1\right] \quad \text{for } k=0,$$
$$f^* = \frac{h}{3b}\left[(1+h/(3b))\ln(1+3b/h)-1\right] \quad \text{for } k\to\infty.$$

These three cases are plotted in Figure 10.26 and show, as expected, that the correction factor is always less than one; the no-slip case corresponds to $f^* = p^* = 1$. Also, both correction factors depend on the length scale ratios, namely h/b and $h/[(k+1)b]$. In the limit of very small gap, the case of

$f^* \to 0$ (corresponding to $k > -1$) represents a configuration of two bubbles approaching each other, while the case of $f^* \to 1/4$ (corresponding to $k = -1$) represents the flow resistance for a hydrophilic sphere interacting with a bubble.

In the standard Reynolds theory ($f^* = 1$) the hydrodynamic resistance is inversely proportional to the gap and diverges for $h \to 0$. However, the new physical result in the solutions of Vinogradova is for two hydrophobic surfaces, i.e., $k > -1$ and $h \to 0$, where the friction coefficient

$$\frac{f^*}{h} = -\frac{2}{C-B}\left[(1-A/B)\ln B/h - (1-A/C)\ln C/h\right]$$

depends logarithmically on h and is inversely proportional to the slip length b. The above result is valid for $h \ll C < B$. This dependence is more clearly seen for the case in which A and C are approximately of the same order of magnitude. In this case, (Vinogradova, 1995) has derived that

$$\frac{f^*}{h} = \frac{1}{3b}\ln\left(\frac{6b}{h}\right),$$

which again shows the logarithmic dependence on the gap h.

The above formulation for two spheres has been extended to *general curved* hydrophobic surfaces by (Vinogradova, 1996). The results are very similar to those of the case of two spheres. For example, the resistance force is given by

$$F_z = -\frac{3\pi\mu v}{hI_1\sqrt{I_2}}f^*, \tag{10.13}$$

where f^* is defined by the same expression of equation (10.12), but the geometry is now described by the curvatures of the two surfaces as follows:

$$I_1 = \frac{1}{2}\left[\frac{1}{R_1^-} + \frac{1}{R_1^+} + \frac{1}{R_2^-} + \frac{1}{R_2^+}\right],$$

$$I_2 = \frac{1}{4}\left[\frac{1}{R_1^- R_1^+} + \frac{1}{R_2^- R_2^+} + \sin^2\phi\left(\frac{1}{R_2^+ R_1^+} + \frac{1}{R_2^- R_1^-}\right) + \cos^2\phi\left(\frac{1}{R_2^- R_1^+} + \frac{1}{R_2^+ R_1^-}\right)\right].$$

Here R^+ and R^- denote the maximum and minimum principal radii of the surface, and thus I_1 and I_2 are the *mean* and *Gaussian* curvatures of the effective surface, respectively. Also, ϕ defines the orientation of the two coordinate systems attached to the two surfaces. For example, we can consider the interaction of a *sphere with a plane*, a case typical in the surface force apparatus, in which case we obtain $I_1 = 1/R$ and $I_2 = 1/(4R^2)$. Similarly, we can model two *crossed cylinders* for which $R_2^+, R_1^+ \to \infty$ and $\phi = \pi/2$, so the two invariants are

$$I_1 = \frac{1}{2}\left(\frac{1}{R_2^-} + \frac{1}{R_1^-}\right) \quad \text{and} \quad I_2 = \frac{1}{4R_2^- R_1^-}.$$

The reader can try to determine the two invariants for the case of two hydrophobic cylinders with aligned axes for which $\phi = 0$.

The analytical models of Vinogradova have been used with success in fitting the force curves in several SFA measurements, e.g., (Zhu and Granick, 2001; Zhu and Granick, 2002), but the expression for f^* does not depend on the shear rate. However, in several SFA experiments it was shown convincingly that there is a strong dependence of the response on the driving speed, and thus these data do not agree with Vinogradova's theory (Spikes and Granick, 2003). To this end, a new model was proposed by (Spikes and Granick, 2003) based on the observation that the experimental results may represent *onset of slip* at a fixed shear stress $\tau_{\rm co}$ rather than slip at a constant slip length b. Because in the SFA a sphere interacts with a plane, the surface shear stress is zero at the center and also away from it with maximum values in between; see Figure 10.19. This, in turn, implies that there exists an annular region around the contact point where slip occurs. The proposed new model in (Spikes and Granick, 2003), combines both this critical shear stress and the slip at constant b, so the shear stress when boundary slip occus is

$$\tau_c = \tau_{\rm co} + \frac{\mu}{b} v_s.$$

The corresponding pressure gradient for the case of one slippery surface only is

$$\frac{dp}{dr} = -\min\left\{\frac{6\mu W r}{h^3}, \left(\frac{6\mu W r}{h^3} - \frac{6b}{(h+4b)}\left(-\frac{\tau_{\rm co}}{h} + \frac{3\mu W r}{h^3}\right)\right)\right\},$$

where min denotes the minimum of the two quantities, and W is the squeeze velocity; h is the gap height at radial distance r. The influence of $\tau_{\rm co}$ may not be realized in some applications, including cases in which it is constant, as in microchannel pressure-driven or Couette flow. However, it provides a correction for low shear stress configurations and also for the surface force apparatus and the atomic force microscope as well as in surfaces with roughness.